

Non-resonant relaxation of anisotropic globular clusters

Kerwann Tep¹, Jean-Baptiste Fouvry¹ and Christophe Pichon^{1,2}

¹ CNRS and Sorbonne Université, UMR 7095, Institut d’Astrophysique de Paris, 98 bis Boulevard Arago, F-75014 Paris, France

² IPHT, DRF-INP, UMR 3680, CEA, Orme des Merisiers Bât 774, F-91191 Gif-sur-Yvette, France

12 January 2022

ABSTRACT

Globular clusters are dense stellar systems whose core slowly contracts under the effect of self-gravity. The rate of this process was recently found to be directly linked to the initial amount of velocity anisotropy: tangentially anisotropic clusters contract faster than radially anisotropic ones. Furthermore, initially anisotropic clusters are found to generically tend towards more isotropic distributions during the onset of contraction. Chandrasekhar’s “non-resonant” (NR) theory of diffusion describes this relaxation as being driven by a sequence of local two-body deflections along each star’s orbit. We explicitly tailor this NR prediction to anisotropic clusters, and compare it with N -body realisations of Plummer spheres with varying degrees of anisotropy. The NR theory is shown to recover remarkably well the detailed shape of the orbital diffusion and the associated initial isotropisation, up to a global multiplicative prefactor which increases with anisotropy. Strikingly, a simple effective isotropic prescription provides almost as good a fit, as long as the cluster’s anisotropy is not too strong. For these more extreme clusters, accounting for long-range resonant relaxation may be necessary to capture these clusters’ long-term evolution.

Key words: Diffusion - Gravitation - Galaxies: kinematics and dynamics

1 INTRODUCTION

Understanding the long-term evolution of globular clusters is a long-standing problem in stellar dynamics (Hénon 1961; Harris & Racine 1979; Spitzer 1987). Not only is the dynamics of globular clusters interesting *per se* (see, e.g., Lightman & Shapiro 1978; Harris 1991; Meylan & Heggie 1997; Brodie & Strader 2006), but it is also the archetype for the relaxation of a (weakly) collisional self-gravitating system with a simple integrable configuration (see, e.g., Chavanis 2013a, for a review).

In Chandrasekhar (1943)’s picture, the velocity of a given test star undergoes a series of weak, local, and uncorrelated kicks from each field star it encounters, a process that we coin “non-resonant relaxation” (NR). Once these deflections accumulated along the stars’ underlying unperturbed orbits, NR provides us with the classical picture for long-term relaxation in spherical clusters (Heggie & Hut 2003). In practice, NR is rather straightforward to implement for isotropic clusters and has been extensively used to describe their long-term evolution (see, e.g., Vasiliev 2015, for a review). The same approach was also recently updated via the (inhomogeneous) Balescu–Lenard equation (Heyvaerts 2010; Chavanis 2012) to account for gravitational wakes and large-scale resonances within the globular clusters (Hamilton et al. 2018; Fouvry et al. 2021). Overall these non-local effects were, somewhat surprisingly, found to be of small relevance for such isotropic spheres. Moving away from isotropy, one could expect that more coherent motions within the cluster, e.g., via velocity anisotropies, could affect these

systems’ long-term evolution. In this paper, we wish to quantify the extent to which NR still applies for such systems.

Longaretti & Lagoute (1997); Kim et al. (2008); Hong et al. (2013) studied the impact of rotation on globular clusters using N -body simulations and Fokker–Planck models. They concluded that core collapse was accelerated in clusters with a non-zero total angular momentum. For non rotating, but anisotropic clusters, Cohn (1979) devised an orbit-averaged Fokker–Planck equation to integrate self-consistently the evolution of a spherical star cluster. In that paper, the velocity diffusion coefficients are computed using a pseudo-isotropic distribution function, i.e. at a fixed radius, the test star is scattered by a locally isotropic background of perturbers. This approach was further refined in the Fokker–Planck simulations of Drukier et al. (1999) to carefully treat the effects of velocity-space anisotropy. More recently, Breen et al. (2017) used direct N -body simulations to investigate the relaxation of isolated equal-mass star clusters, primarily focusing on the effects of primordial velocity anisotropies. Interestingly, collapse is found to be swifter as the model becomes more and more tangentially anisotropic.

The purpose of our paper is to extend the NR theory to anisotropic clusters and to model the result of Breen et al. (2017). The comparison to tailored simulations also allows us to assess the relative performance of the pseudo-isotropic computation presented in Cohn (1979). The paper is organised as follows. In §2 we tailor Chandrasekhar’s NR theory to anisotropic spherical clusters, then in §3 we apply this approach to Plummer spheres, while we discuss our results and conclude in §4.

2 NON-RESONANT RELAXATION

We consider a self-gravitating globular cluster composed of N stars of individual mass $m_b = M/N$, with M the cluster's total mass. Assuming that this cluster is in a quasi-stationary equilibrium, we characterise its phase-space statistics using the total DF, $F_{\text{tot}} = F_{\text{tot}}(\mathbf{r}, \mathbf{v})$, with \mathbf{r} the position and \mathbf{v} the velocity, normalised so that $\int d\mathbf{r} d\mathbf{v} F_{\text{tot}} = M$.

2.1 Local velocity diffusion coefficients

As a result of the cluster's finite number of constituents, a given test star of mass m and velocity \mathbf{v} , embedded in such a noisy environment will irreversibly see its velocity diffuse. This long-term relaxation is driven by pairwise encounters, a process that we call non-resonant (NR) relaxation. More precisely, assuming that the deflection is local and following §7.4.4 of Binney & Tremaine (2008) (see also Chavanis (2013b) for a review), the test star's velocity will locally diffuse according to the first- and second-order velocity diffusion coefficients

$$\langle \Delta v_i \rangle = 4\pi G^2 (m + m_b) \ln \Lambda \frac{\partial h}{\partial v_i}, \quad (1a)$$

$$\langle \Delta v_i \Delta v_j \rangle = 4\pi G^2 m_b \ln \Lambda \frac{\partial^2 g}{\partial v_i \partial v_j}, \quad (1b)$$

where i and j run over the three directions of the coordinate system. In that expression, G is the gravitational constant and $\ln \Lambda$ stands for the Coulomb logarithm stemming from the heuristic regularisation of local and far-away encounters. Finally, equation (1) involves the Rosenbluth potentials (Rosenbluth et al. 1957), which read

$$h(\mathbf{r}, \mathbf{v}) = \int d\mathbf{v}' \frac{F_{\text{tot}}(\mathbf{r}, \mathbf{v}')}{|\mathbf{v} - \mathbf{v}'|}, \quad (2a)$$

$$g(\mathbf{r}, \mathbf{v}) = \int d\mathbf{v}' F_{\text{tot}}(\mathbf{r}, \mathbf{v}') |\mathbf{v} - \mathbf{v}'|. \quad (2b)$$

While fully generic, equations (1) and (2) are typically further simplified by assuming spherical symmetry and a locally isotropic velocity distribution (see, e.g., Hénon 1958). In that limit, one imposes $F_{\text{tot}}(\mathbf{r}, \mathbf{v}) = F_{\text{tot}}(r, v)$, with $v = |\mathbf{v}|$, $r = |\mathbf{r}|$, and all the integrals from equation (2) become one-dimensional. One key goal of our paper is to assess the validity of this isotropy assumption.

2.2 Anisotropic diffusion coefficients

For a non-rotating anisotropic DF with spherical symmetry, one generically has $F_{\text{tot}}(\mathbf{r}, \mathbf{v}) = F_{\text{tot}}(r, v_r, v_t)$, where v_r and v_t are respectively the radial and tangential velocities, satisfying $v^2 = v_r^2 + v_t^2$.

In §A, we show that within these coordinates the diffusion coefficients from equation (1) are fully captured by

$$\langle \Delta v_{\parallel} \rangle = 4\pi G^2 (m + m_b) \ln \Lambda \left(\frac{v_r}{v} \frac{\partial h}{\partial v_r} + \frac{v_t}{v} \frac{\partial h}{\partial v_t} \right), \quad (3a)$$

$$\begin{aligned} \langle (\Delta v_{\parallel})^2 \rangle &= 4\pi G^2 m_b \ln \Lambda \left[\left(\frac{v_r}{v} \right)^2 \frac{\partial^2 g}{\partial v_r^2} + \frac{2v_r v_t}{v^2} \frac{\partial^2 g}{\partial v_r \partial v_t} \right. \\ &\quad \left. + \left(\frac{v_t}{v} \right)^2 \frac{\partial^2 g}{\partial v_t^2} \right], \end{aligned} \quad (3b)$$

$$\begin{aligned} \langle (\Delta v_{\perp})^2 \rangle &= 4\pi G^2 m_b \ln \Lambda \left[\left(\frac{v_t}{v} \right)^2 \frac{\partial^2 g}{\partial v_r^2} - \frac{2v_r v_t}{v^2} \frac{\partial^2 g}{\partial v_r \partial v_t} \right. \\ &\quad \left. + \left(\frac{v_r}{v} \right)^2 \frac{\partial^2 g}{\partial v_t^2} + \frac{1}{v_t} \frac{\partial g}{\partial v_t} \right], \end{aligned} \quad (3c)$$

where Δv_{\parallel} and Δv_{\perp} stand respectively for the local velocity deflections along and perpendicular to the star's motion. For a fully isotropic cluster, those reduce to the already known formulae (see, e.g., equation L.25 in Binney & Tremaine 2008), as detailed in §B.

The next step of the calculation is to explicitly compute all the gradients of the Rosenbluth potentials that appear in the r.h.s. of equation (3). In §C, owing to an appropriate change of variables, we rewrite these gradients as simple three-dimensional integrals over velocity space. Equation (3) used in conjunction with equations (C5)–(C13) are key results of the present work. Importantly, these final expressions do not involve any velocity denominator nor any gradient of the cluster's DF. In §D, we also check these new expressions by deriving them independently from the homogeneous Landau equation.

2.3 Orbit-average and secular evolution

Because the specific energy and angular momentum of the test star, (E, L) , are simple functions of (r, v_r, v_t) , it is straightforward to compute the local diffusion coefficients in (E, L) from the local velocity diffusion coefficients, as detailed in §F1. These local coefficients are then orbit-averaged over the unperturbed motion of the test star (see, e.g., §7.4.2 in Binney & Tremaine 2008) by writing

$$D_E = \frac{1}{T} \int_0^T dt \langle \Delta E \rangle, \quad (4)$$

with T the test star's radial period, and similarly for the other diffusion coefficients. In equation (4), we emphasise that the integrand, $\langle \Delta E \rangle$, is evaluated in $(r(t), v_r(t), v_t(t))$ as one follows the test star's orbit. We defer to §F2 the presentation of an explicit and numerically stable scheme to perform this orbit average.

Finally, we rewrite the diffusion coefficients in action space, namely $\mathbf{J} = (J_r, L)$ with J_r the radial action, following §F3. Rather than focusing on the relaxation of a single test star, we can treat the whole globular cluster as a large collection of test stars. The cluster's orbital distribution is governed by the reduced DF,

$$F(\mathbf{J}) = 2L F_{\text{tot}}(\mathbf{J}), \quad (5)$$

which is proportional to the density of stars in \mathbf{J} -space. The long-term evolution of $F(\mathbf{J})$ follows from the Fokker–Planck equation (see, e.g., §7.4 in Binney & Tremaine 2008) which reads here

$$\begin{aligned} \frac{\partial F(\mathbf{J})}{\partial t} &= -\frac{\partial}{\partial \mathbf{J}} \cdot \mathbf{F}(\mathbf{J}) \\ &= -\frac{\partial}{\partial \mathbf{J}} \cdot \left[\mathbf{D}_1(\mathbf{J}) F(\mathbf{J}) - \frac{1}{2} \frac{\partial}{\partial \mathbf{J}} \cdot \left[\mathbf{D}_2(\mathbf{J}) F(\mathbf{J}) \right] \right], \end{aligned} \quad (6)$$

where $\mathbf{F}(\mathbf{J})$ is the diffusion flux in action space, and the first- and second-order diffusion coefficients read

$$\mathbf{D}_1(\mathbf{J}) = \begin{pmatrix} D_{J_r} \\ D_{L} \end{pmatrix}, \quad \mathbf{D}_2(\mathbf{J}) = \begin{pmatrix} D_{J_r J_r} & D_{J_r L} \\ D_{J_r L} & D_{L L} \end{pmatrix}. \quad (7)$$

The relaxation rate $\partial F / \partial t$ in equation (6) then specifies the dynamical evolution of any orbit-averaged quantity within the system.

3 APPLICATION TO PLUMMER SPHERES

So far, our derivations apply to any spherically symmetric, non-rotating anisotropic globular cluster. Hereafter, we focus on the Plummer sphere to provide a quantitative assessment of the impact of anisotropy on secular evolution.

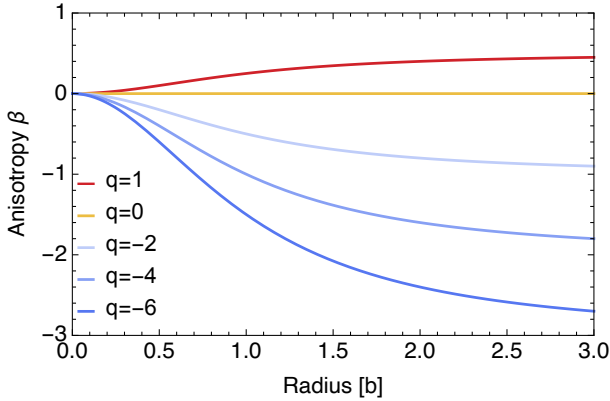


Figure 1. Anisotropy parameter $\beta(r)$ of the considered equilibrium DFs (§E) as a function of the radius in units $b = 1$. Here, $q = 0$ stands for the isotropic equilibrium while $q < 0$ (resp. $q > 0$) are tangentially (resp. radially) anisotropic equilibria.

3.1 The Plummer model

The Plummer potential reads

$$\psi(r) = -\frac{GM}{\sqrt{b^2 + r^2}}, \quad (8)$$

with M the cluster’s total mass and b its scale radius. In the following, for the sake of simplicity, we use physical units so that $G = M = b = 1$, and consider clusters composed of $N = 10^5$ stars. Following Giersz & Heggie (1994), we also set the value of the Coulomb logarithm to $\ln \Lambda = \ln(0.11 N)$.

In order to compute orbit-averaged diffusion coefficients in the case of a Plummer potential, we rewrite equation (4) as

$$D_E = \frac{2}{T} \int_{-1}^1 du \Theta(u) \langle \Delta E \rangle. \quad (9)$$

Here, u stands for an explicit effective anomaly whose weight function $\Theta(u)$ is always well-defined, numerically stable, and explicit, as detailed in §F2. The same anomaly is also used to rewrite the orbit-averaged diffusion coefficients in (J_r, L) -space, see §F3.

In order to vary the cluster’s velocity anisotropy, we consider the same series of equilibria as in Breen et al. (2017). As detailed in §E, the considered DF depends on a parameter q so that its anisotropy parameter β varies as

$$\beta(r) = 1 - \frac{\sigma_t^2}{2\sigma_r^2} = \frac{q}{2} \frac{r^2}{1 + r^2}, \quad (10)$$

with σ_t and σ_r the local tangential and radial velocity dispersions. As illustrated in Fig. 1, the case $q = 0$ corresponds to the isotropic equilibrium, while $q < 0$ (resp. $q > 0$) corresponds to tangentially (resp. radially) anisotropic equilibria. Given the radial dependence of equation (10), we also point out that, for a fixed value of q , the anisotropy is the largest in the cluster’s outskirts.

3.2 Contraction and isotropisation

Our goal is to investigate the impact of anisotropy on the cluster’s relaxation. Using direct N -body simulations, detailed in §G, we illustrate this dependence in Fig. 2 with the evolution of the cluster’s core radius as one varies q . As already pointed out in Breen et al. (2017) (fig. 4 therein), the more tangentially anisotropic the cluster, the faster its initial contraction.

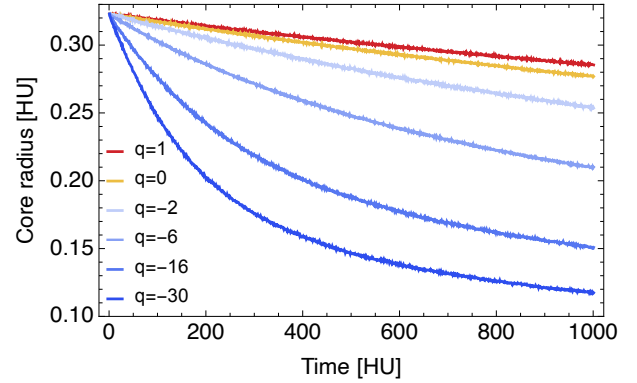


Figure 2. Ensemble-averaged evolution of the cluster’s core radius as a function of time from direct N -body simulations, as one varies the anisotropy parameter q . We refer to §G for the details of the numerical setup and the definition of the Hénon units (HU). Larger negative values of q , i.e. more tangentially anisotropic clusters, are unambiguously associated with a faster initial evolution.

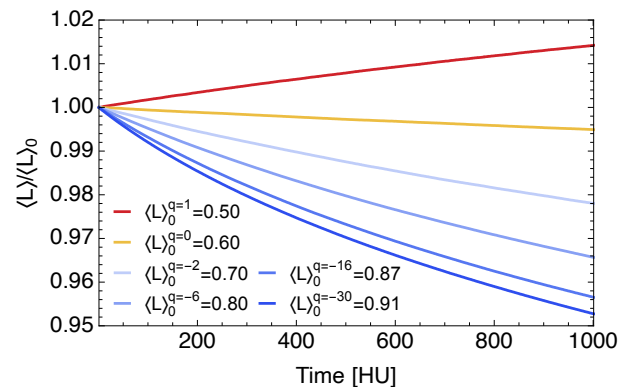


Figure 3. Ensemble-averaged evolution of the mean angular momentum norm, $\langle L \rangle$ (rescaled by its initial value $\langle L \rangle_0$) as one varies the anisotropy parameter q , using the same simulations as in Fig. 2. Clusters isotropise throughout their relaxation, i.e. $\langle L \rangle$ increases for radially anisotropic clusters and decreases for tangentially anisotropic ones. In addition, for $q < 0$, the stronger the tangential anisotropy, the faster the initial isotropisation.

Using the same simulations, we also investigate the time evolution of the clusters’ average angular momentum modulus

$$\langle L \rangle = \frac{(2\pi)^3}{M} \int d\mathbf{J} L F(\mathbf{J}), \quad (11)$$

as illustrated in Fig. 3. Similarly to fig. 7 of Breen et al. (2017), we recover here that the clusters’ relaxations drive them towards more isotropic distribution. Indeed, radially anisotropic clusters (i.e. $q > 0$) see their average angular momentum grow, i.e. orbits become on average more circular, while tangentially anisotropic clusters (i.e. $q < 0$) see their average angular momentum decrease, i.e. orbits become more radial. Finally, as in Fig. 2, we recover that the more tangentially anisotropic a cluster, the faster its initial isotropisation.

We are now in a position to assess how well the anisotropic NR theory from §2 can predict these trends.

3.3 Comparing NR and N -body evolution

In the limit where nearby deflections drive the cluster’s relaxation, its long-term evolution is governed by the Fokker–Planck equation (6), which predicts the rate of change $\partial F / \partial t$ in action space.

In Fig. 4, we compare the contours of $\partial F/\partial t$ as predicted by the anisotropic NR theory from equation (3) with those measured in N -body simulations, for various initial velocity anisotropies¹. In Fig. 4, it is remarkable that the NR maps and the N -body measurements are so similar, up to an overall prefactor which appears to weakly depend on the considered actions. This prefactor reflects the fact that NR theory poorly accounts for far-away encounters, that only resonant relaxation captures (see, e.g., Fouvry et al. 2021).

In order to better quantify the overall amount by which the NR prediction overestimates the N -body prediction, we define the average ratio

$$\frac{\text{NR}}{N\text{-BODY}} = \frac{\int d\mathbf{J} F(\mathbf{J}) |\partial F/\partial t|_{\text{NR}}}{\int d\mathbf{J} F(\mathbf{J}) |\partial F/\partial t|_{N\text{-BODY}}}, \quad (12)$$

where the rates of change, $\partial F/\partial t$, are inferred from Fig. 4. In Fig. 5, we present the dependence of this ratio as a function of the cluster's anisotropies. In that figure, we find that for an isotropic velocity distribution, i.e. $q = 0$, NR overestimates the N -body measurement by a factor ~ 1.4 . This is fully compatible with the previous measurements from Theuns (1996) and Fouvry et al. (2021) that observed ratios of order $\sim 1.5 - 2$ respectively in isotropic King spheres and isotropic isochrone clusters. Interestingly, in Fig. 5, we recover that the ratio from equation (12) worsens as the cluster get more tangentially anisotropic: for $q = -30$, the NR theory overestimates the diffusion rate by a factor ~ 3 .

In Fig. 6, we provide an alternative representation of the diffusion predicted by NR. In that figure, we represent the field lines of the diffusion flux sourced by equation (6), i.e. the direction along with orbits flow in action space. Here, we recover that the NR diffusion flux reshuffles the system towards a more isotropic distribution: radially anisotropic clusters see their orbits diffuse toward more circular orbits, while tangentially anisotropic clusters see their orbits become more radial on average.

Building upon equation (11), we can further quantify this isotropisation by estimating the initial time variation of the total angular momentum norm within the sphere via

$$\frac{d\langle L \rangle}{dt} = \frac{(2\pi)^3}{M} \int d\mathbf{J} L \frac{\partial F}{\partial t}. \quad (13)$$

In Fig. 7, we compare $d\langle L \rangle/dt$ as predicted by the NR theory (using Fig. 4) and as measured in the N -body simulations (using Fig. 3). In that figure, we confirm once again that anisotropic clusters tend to isotropise during their relaxation. Indeed, one finds $d\langle L \rangle/dt > 0$ for radially anisotropic clusters ($q > 0$), i.e. orbits tend to get more circular, while one has $d\langle L \rangle/dt < 0$ for tangentially anisotropic clusters ($q < 0$), i.e. orbits become more radial. Similarly to Fig. 5, we also recover that the NR prediction systematically overestimates the N -body measurement by a factor that grows as the cluster's initial anisotropy increases.

4 DISCUSSION

4.1 Pseudo-Isotropic diffusion

The anisotropic diffusion coefficients involve three-dimensional integrals (see equations C5–C13). This is numerically more demanding than the isotropic ones which involve one-dimensional inte-

grals (see equation B7). In the view of benefiting from these simpler expressions, Cohn (1979) introduced the concept of a locally isotropised DF.

Following equation (16) of Cohn (1979) (see also equation 4.81 in Binney & Tremaine 2008), we introduce the pseudo-isotropic (P-Iso) DF²

$$F_{\text{tot}}^{\text{P-Iso}}(r, E) = \int_0^{\frac{\pi}{2}} dx \sin x F_{\text{tot}}(E, \sin x L_{\text{max}}), \quad (14)$$

with $L_{\text{max}}(r, E) = \sqrt{2r^2(E - \psi(r))}$ the maximum angular momentum possible for a bound orbit of energy E going through the radius r . Importantly, following this local average the pseudo-isotropic DF, $F_{\text{tot}}^{\text{P-Iso}}$, only depends on the energy E .

In Fig. 8, we compare the cluster's anisotropic and pseudo-isotropic DFs for various radii and various anisotropies. As already highlighted in Fig. 1, for a fixed value of q , as one moves closer to the cluster's centre, the local anisotropy diminishes so that the anisotropic and pseudo-isotropic DFs closely follow one another. For a fixed radius r , as the anisotropy parameter q gets away from $q = 0$, the local anisotropy increases, hence increasing the differences between the two DFs.

Once the pseudo-isotropic DF is known, it can straightforwardly be used in equation (B5) to estimate the velocity diffusion coefficients via (rapid) one-dimensional integrals (equation B7). This is what we present in Fig. 9, where we compare the contours of $\partial F/\partial t$ as predicted by the fully anisotropic diffusion coefficients (computed via equation 3) and their pseudo-isotropic analogs (computed via equation B5). In that figure, we note that, for the anisotropies considered here, the differences between the two maps are minor. This follows in fact from Fig. 1, where we noted that as one moves closer to the cluster's core, the anisotropy gets reduced, hence the similitude of the two maps reported in Fig. 9 which focus on the cluster's central region. We reach the same conclusion in §I by noting that the local velocity deflections accumulated along a test star's motion in the cluster's core only marginally differ between the anisotropic and pseudo-isotropic predictions (see Fig. 11).

In order to better compare these two predictions, following equation (12), we compute the respective ratio of the NR and P-Iso predictions through

$$\frac{\text{NR}}{\text{P-Iso}} = \frac{\int d\mathbf{J} F(\mathbf{J}) |\partial F/\partial t|_{\text{NR}}}{\int d\mathbf{J} F(\mathbf{J}) |\partial F/\partial t|_{\text{P-Iso}}}, \quad (15)$$

which is represented in Fig. 10. In that figure, we recover that for the anisotropy parameters q considered here, the two maps typically differ, at most, by $\sim 5\%$. As expected, as one increases the cluster's anisotropy, the mismatch between the two predictions increases. Finally, we point out that this similitude between NR and P-Iso is a pleasant numerical news. Indeed, rather than having to go through the three-dimensional NR integrals from equations (C5)–(C13), the P-Iso prediction requires, in essence, two-dimensional integrals by computing first the pseudo-isotropic DF from equation (14) and subsequently the associated isotropic diffusion coefficients from equation (B7).

¹ See §H for even more anisotropic distributions.

² Equation (14) follows from equation (16) of Cohn (1979) via the change of variable $R = \sin^2 x R_{\text{max}}$, with R and R_{max} defined in Cohn (1979).

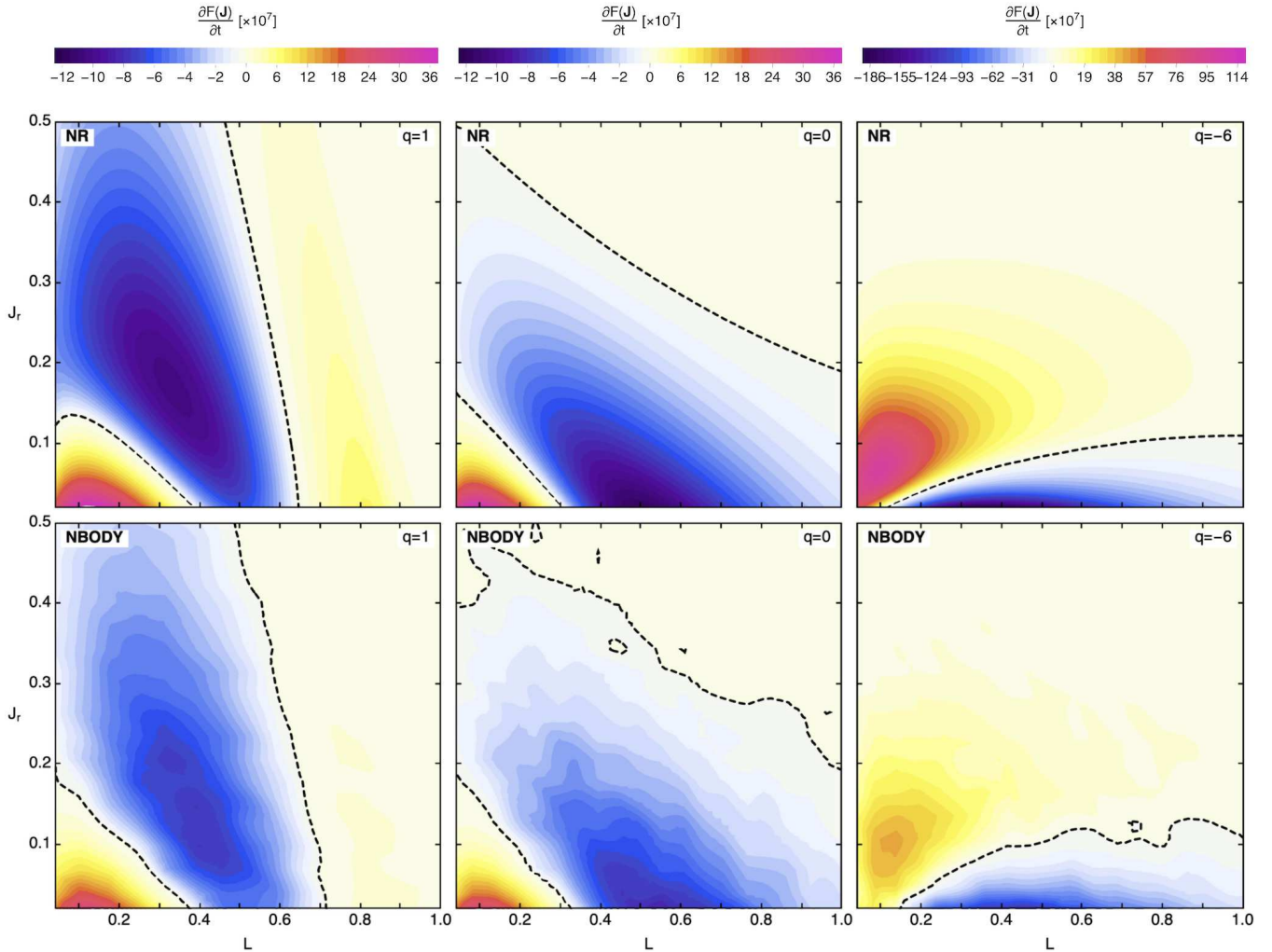


Figure 4. Illustration of the local relaxation rate, $\partial F/\partial t$, for various values of the anisotropy parameter q (left to right), as predicted by the anisotropic NR prediction (top, §2.2) and measured in direct numerical simulations (bottom, §G). There is a qualitative agreement between the NR predictions and the N -body measurement, up to an overall prefactor depending on the level of anisotropy q (see also Figs. 5 and H1).

4.2 Conclusion

We tailored Chandrasekhar’s NR theory to compute the local velocity diffusion coefficients in non-rotating anisotropic spherical clusters. We implemented explicitly these expressions, now distributed through a publicly available code.

We subsequently applied the present anisotropic NR theory to a series of anisotropic Plummer spheres. Building upon Breen et al. (2017), we reached two main conclusions. First, the NR prediction matches qualitatively direct N -body measurements (see Fig. 4) up to an overall prefactor $\sim 1.4 - 2$ that worsens as the initial anisotropy increases (see Fig. 5). This match between theory and simulations shows that NR captures the more rapid compression of tangentially anisotropic globular cluster compared to radially anisotropic ones (see Fig. 2), though the incorrect prefactor suggests that NR misestimates the contributions from large-scale encounters. Second, we pointed out that NR also drives initially an isotropisation of the clusters (see, e.g., Fig. 6).

Finally, following Cohn (1979), we investigated the errors introduced by locally isotropising the DF of the perturbers (see equation 14), an approach that we coined “pseudo-isotropic”. For the

class of anisotropic clusters considered, we emphasised that the limited extent of anisotropy in the inner regions (see Fig. 8) led to differences of order $\lesssim 5\%$ with respect to the fully anisotropic calculation. As such, for the clusters considered here, we confirmed that the anisotropy of the perturbers’ DF, via $F_{\text{tot}}(\mathbf{r}, \mathbf{v}')$ in equation (2), plays a much less important role than the anisotropy in the test particles’ DF, via $F(\mathbf{J})$ in equation (6).

4.3 Perspectives

Having computed $\partial F/\partial t$ from kinetic theory (Fig. 4), we could in principle predict the initial time evolution of more traditional quantities such as the anisotropy parameter $\beta(r)$ (Fig. 1) or the core radius $R_c(t)$ (Fig. 2) at the cost of accounting appropriately for the self-consistent update of the cluster’s mean potential. Ultimately, following for example Vasiliev (2015), one could also hope to integrate self-consistently the time evolution of the whole cluster as driven by the present NR theory. Figure 6 emphasised that local deflections naturally tend to isotropise the cluster’s DF. Given this increased isotropy, one may expect that the pseudo-isotropic prescription from equation (14) will become more relevant as the

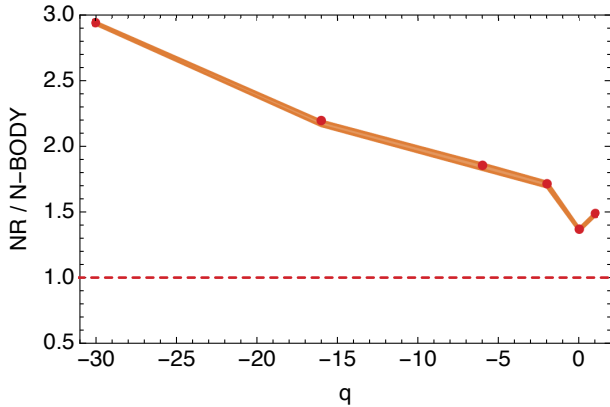


Figure 5. Ratio of the diffusion rate of the NR theory and N -body predictions (equation 12) as a function of the cluster’s anisotropy parametrised by q . The dots corresponds to anisotropies for which N -body simulations were performed, and the contours correspond to the 16% and 84% level lines over the available realisations. For the isotropic cluster ($q = 0$), the NR theory overestimates the diffusion rate by a factor ~ 1.4 , which worsens as the cluster becomes more and more anisotropic.

relaxation occurs. Of course this would deserve to be investigated in more detail, following for example fig. 7 of Breen et al. (2017).

In §3, we restricted our analysis to Plummer potentials. Nevertheless the generic derivation presented in §2 should translate to any “reasonable” core potential, provided one has access to its distribution function, e.g., following the method from Dejonghe (1987). It would also be of interest to investigate truncated, cuspy, or even rotating spheres, since the clusters’ orbital structure impacts both their linear and long-term responses. In order to alleviate some of the numerical challenges, it would be worthwhile to find an efficient way of carrying out the orbit-averages using numerically stable effective anomalies (as in §F2) for each such potential.

As illustrated in Fig. 5, the NR theory and the N -body measurements still present an overall multiplicative discrepancy. It most probably arises from the fact that NR does not capture accurately the contribution from far-away encounters, collective effects, and non-local resonances. Following Fouvy et al. (2021), it would be of interest to investigate the resonant relaxation (RR) of spherical clusters with various levels of anisotropy. This should ultimately pave the way to predict ab initio the effective Coulomb logarithm $\ln \Lambda$ in equation (1). This will be the topic of future work.

Data Distribution

The data underlying this article is available through reasonable request to the author. The code for the anisotropic NR diffusion coefficient is available at the following URL: <https://github.com/KerwannTEP/CAT>.

ACKNOWLEDGEMENTS

This work is partially supported by grant Segal ANR-19-CE31-0017 of the French Agence Nationale de la Recherche, and by the Idex Sorbonne Université. We are grateful to M. Roule and M. Petersen for numerous suggestions during the completion of this work. We thank Stéphane Rouberol for the smooth running of the Infinity cluster, where the simulations were performed.

REFERENCES

- Bar-Or B., Alexander T., 2016, *ApJ*, 820, 129
 Binney J., Tremaine S., 2008, *Galactic Dynamics: Second Edition*. Princeton Univ. Press
 Breen P. G., Varri A. L., Heggie D. C., 2017, *MNRAS*, 471, 2778
 Brodie J. P., Strader J., 2006, *ARA&A*, 44, 193
 Casertano S., Hut P., 1985, *ApJ*, 298, 80
 Chandrasekhar S., 1943, *ApJ*, 97, 255
 Chavanis P.-H., 2012, *Physica A*, 391, 3680
 Chavanis P.-H., 2013a, *Eur. Phys. J. Plus*, 128, 126
 Chavanis P. H., 2013b, *A&A*, 556, A93
 Cohn H., 1979, *ApJ*, 234, 1036
 Dejonghe H., 1987, *MNRAS*, 224, 13
 Drukier G. A., Cohn H. N., Lugger P. M., Yong H., 1999, *ApJ*, 518, 233
 Fouvy J.-B., Hamilton C., Rozier S., Pichon C., 2021, *MNRAS*, 508, 2210
 Giersz M., Heggie D. C., 1994, *MNRAS*, 268, 257
 Hamilton C., Fouvy J.-B., Binney J., Pichon C., 2018, *MNRAS*, 481, 2041
 Harris W. E., 1991, *ARA&A*, 29, 543
 Harris W. E., Racine R., 1979, *ARA&A*, 17, 241
 Heggie D., Hut P., 2003, *The Gravitational Million-Body Problem*
 Hénon M., 1958, *Annales d’Astrophysique*, 21, 186
 Hénon M., 1961, *Annales d’Astrophysique*, 24, 369
 Hénon M. H., 1971, *Ap&SS*, 14, 151
 Heyvaerts J., 2010, *MNRAS*, 407, 355
 Hong J., Kim E., Lee H. M., Spurzem R., 2013, *MNRAS*, 430, 2960
 Kim E., Yoon I., Lee H. M., Spurzem R., 2008, *MNRAS*, 383, 2
 Lightman A. P., Shapiro S. L., 1978, *Rev. Mod. Phys.*, 50, 437
 Longaretti P. Y., Lagoute C., 1997, *A&A*, 319, 839
 Meylan G., Heggie D. C., 1997, *A&ARv*, 8, 1
 Rosenbluth M. N., MacDonald W. M., Judd D. L., 1957, *Phys. Rev.*, 107, 1
 Skowron J., Gould A., 2012, *arXiv*, 1203.1034
 Spitzer L., 1987, *Dynamical evolution of globular clusters*. Princeton Univ. Press
 Theuns T., 1996, *MNRAS*, 279, 827
 Vasiliev E., 2015, *MNRAS*, 446, 3150
 Wang L., Spurzem R., Aarseth S., Nitadori K., Berczik P., Kouwenhoven M. B. N., Naab T., 2015, *MNRAS*, 450, 4070

APPENDIX A: LOCAL DIFFUSION COEFFICIENTS

The local diffusion coefficients, $\langle \Delta v_i \rangle$ and $\langle \Delta v_i \Delta v_j \rangle$, are generically given by equation (1), where $1 \leq i, j \leq 3$ are associated with an arbitrary frame. In order to compute the diffusion coefficients for a generic anisotropic DF, we proceed via two consecutive steps. First, in this Appendix, we generically rewrite the gradients of the Rosenbluth potentials as gradients with respect to the radial and tangential velocities (v_r, v_t). Then, in §C, we explicitly compute these gradients by rewriting them as simple three-dimensional integrals over velocity space.

Assuming that the DF at play is written under the form $F_{\text{tot}}(r, v_r, v_t)$, it is natural to aim at expressing the Rosenbluth potentials as $h(r, v_r, v_t)$ and $g(r, v_r, v_t)$, and compute their gradients with respect to these same coordinates. To do so, we first compute in §A1 the gradients of h and g in an arbitrary coordinate system. Then, in §A2, we apply these generic expressions to a tailored frame to ultimately obtain our main result in equation (3).

A1 Arbitrary frame

As illustrated in Fig. A1, we denote our initial arbitrary frame as $(\mathbf{e}_1, \mathbf{e}_2, \mathbf{e}_3)$, with \mathbf{e}_1 the z -axis. Using standard spherical coordinates, we parametrise the current position of the test particle,

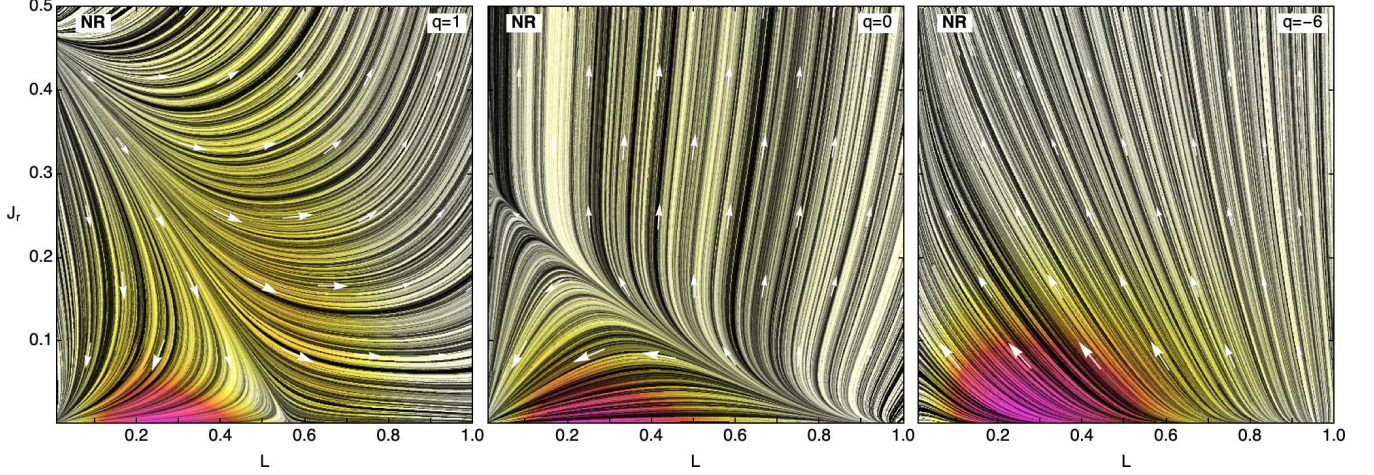


Figure 6. Illustration of the field lines of the diffusion flux, $F(\mathcal{J})$ (see equation 6), as predicted by the NR theory for various anisotropies. The arrows give the average direction along which orbits flow in action space, while red colors are associated with larger flux amplitudes. For anisotropic clusters, i.e. $q \neq 0$, these flows reflect the expected redistribution of orbits towards a more isotropic distribution.

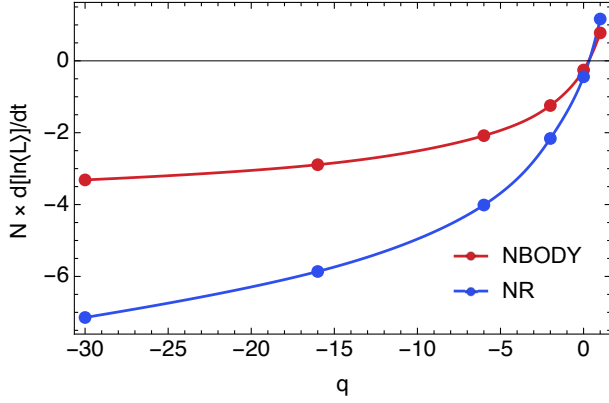


Figure 7. Initial value of $d \ln \langle L \rangle / dt$ as predicted by the NR theory (in blue) and measured in N -body simulations (in red). Anisotropic clusters generically isotropise, i.e. $d \langle L \rangle / dt > 0$ (resp. < 0) in radially (resp. tangentially) anisotropic clusters.

$\mathbf{r} = \mathbf{r}(r, \theta, \phi)$, as

$$r_1 = r \cos \theta, \quad r_2 = r \sin \theta \cos \phi, \quad r_3 = r \sin \theta \sin \phi. \quad (\text{A1})$$

The test particle's velocity $\mathbf{v} = (v_1, v_2, v_3)$ can then be decomposed into its radial and tangential velocities as

$$v_r = \mathbf{v} \cdot \hat{\mathbf{r}} = v_1 \cos \theta + v_2 \sin \theta \cos \phi + v_3 \sin \theta \sin \phi, \quad (\text{A2})$$

$$v_t^2 = v^2 - v_r^2 = v^2 - (v_1 \cos \theta + v_2 \sin \theta \cos \phi + v_3 \sin \theta \sin \phi)^2,$$

with the usual notation $\hat{\mathbf{r}} = \mathbf{r}/|\mathbf{r}|$.

From equation (1), the diffusion coefficients involve the first-order (resp. second-order) gradient of h (resp. g). For $h(\mathbf{r}, \mathbf{v}) = h(r, v_r, v_t)$, one simply has

$$\frac{\partial h}{\partial v_1} = \frac{\partial h}{\partial v_r} \frac{\partial v_r}{\partial v_1} + \frac{\partial h}{\partial v_t} \frac{\partial v_t}{\partial v_1}, \quad (\text{A3})$$

and similarly for $\partial h / \partial v_2$ (resp. $\partial h / \partial v_3$) by the direct replacement $v_1 \rightarrow v_2$ (resp. $v_1 \rightarrow v_3$). In equation (A3), the relevant velocity

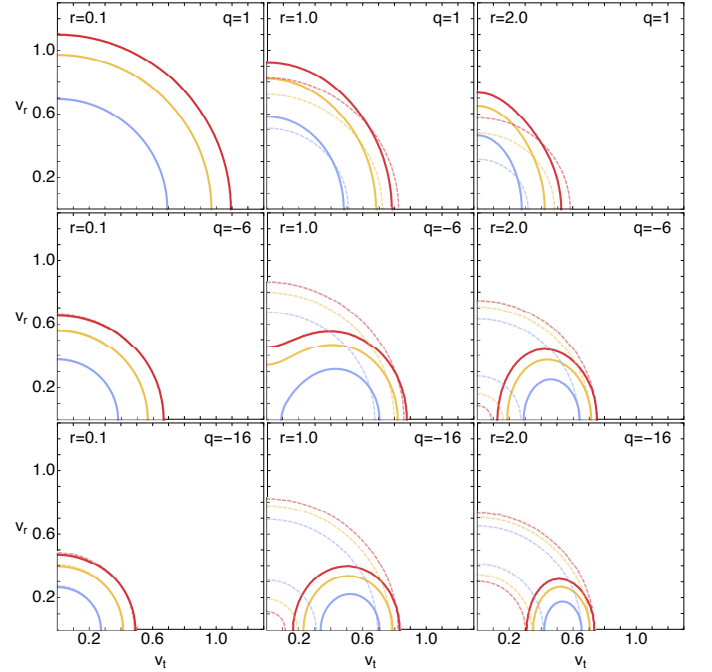


Figure 8. Contour levels of the anisotropic DF (full lines) and pseudo-isotropic DF (dashed lines) in the (v_t, v_r) -space, for various radii (left to right) and various anisotropies (top to bottom). Contours levels correspond to 50% (blue), 20% (orange) and 10% (red) of the DF's maximum at the considered radius. The closer to the cluster's centre, the weaker the anisotropy, and therefore the better the match between the two DFs.

gradients follow from equation (A2) and generically read

$$\frac{\partial v_r}{\partial v_1} = \cos \theta, \quad \frac{\partial v_t}{\partial v_1} = \frac{v_1 - v_r \cos \theta}{v_t}, \quad (\text{A4a})$$

$$\frac{\partial v_r}{\partial v_2} = \sin \theta \cos \phi, \quad \frac{\partial v_t}{\partial v_2} = \frac{v_2 - v_r \sin \theta \cos \phi}{v_t}, \quad (\text{A4b})$$

$$\frac{\partial v_r}{\partial v_3} = \sin \theta \sin \phi, \quad \frac{\partial v_t}{\partial v_3} = \frac{v_3 - v_r \sin \theta \sin \phi}{v_t}. \quad (\text{A4c})$$

Applying the chain rule, we can similarly compute the second-

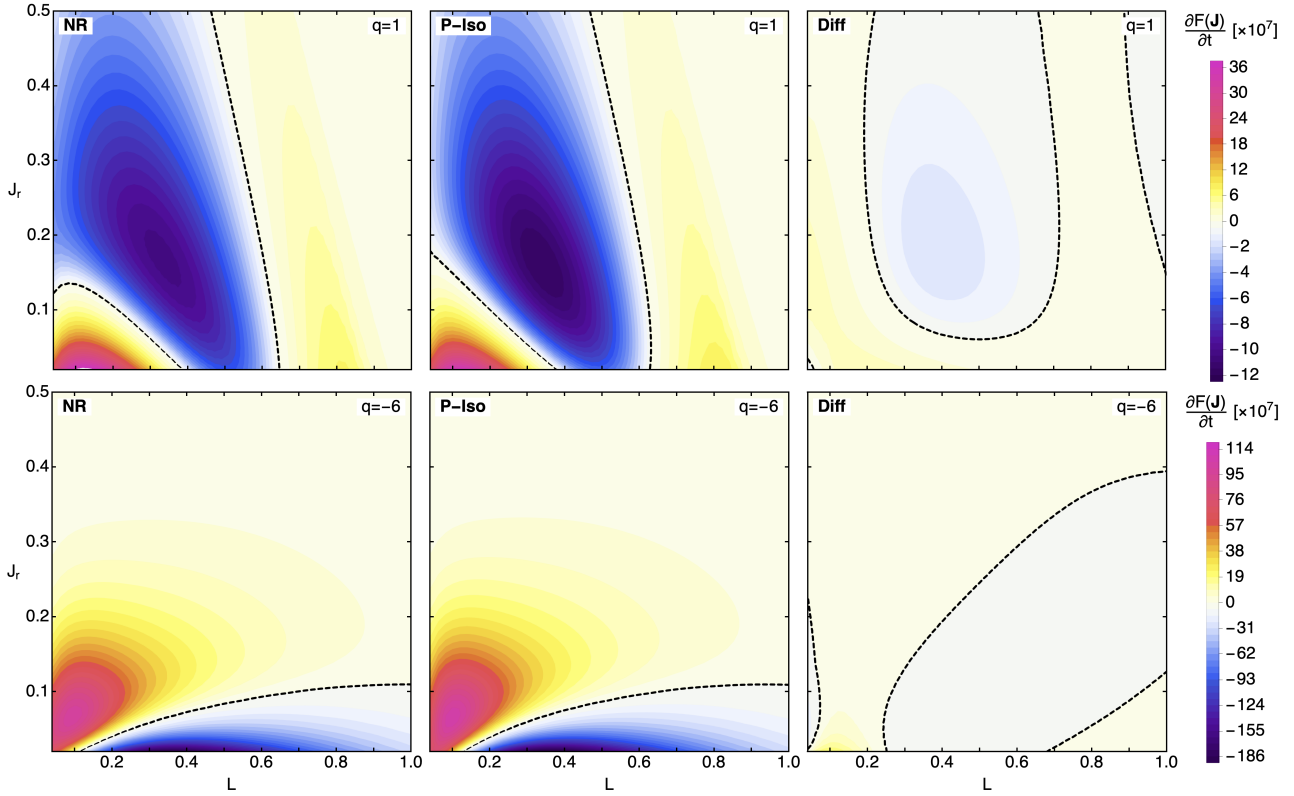


Figure 9. Illustration of the relaxation rate, $\partial F/\partial t$, for two values of the anisotropy parameter q (top and bottom), as predicted by the fully anisotropic NR diffusion coefficients (left), and the pseudo-isotropic ones (middle). The right panel illustrates the difference (“NR minus P-Iso”). For the level of anisotropy considered here, the difference between the two predictions is found to be, at most, $\sim 5\%$.

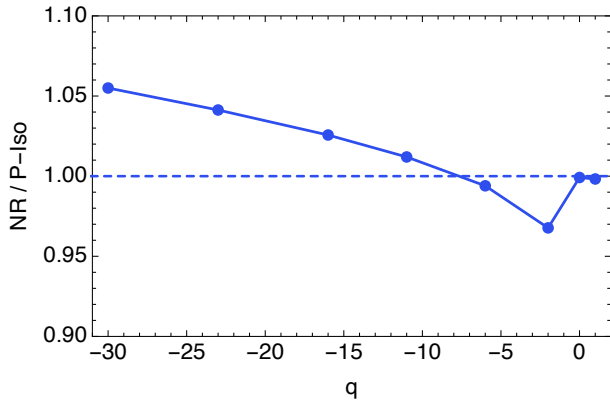


Figure 10. Ratio of the diffusion rate of the NR prediction and the P-Iso one, as defined in equation (15). For an isotropic cluster ($q = 0$) both predictions are, naturally, in agreement, and they start to differ as the cluster becomes more and more anisotropic.

order gradients of $g(\mathbf{r}, \mathbf{v}) = g(r, v_r, v_t)$ via

$$\begin{aligned} \frac{\partial^2 g}{\partial v_1^2} &= \frac{\partial^2 v_r}{\partial v_1^2} \frac{\partial g}{\partial v_r} + \left(\frac{\partial v_r}{\partial v_1}\right)^2 \frac{\partial^2 g}{\partial v_r^2} + \frac{\partial v_r}{\partial v_1} \frac{\partial v_t}{\partial v_1} \frac{\partial^2 g}{\partial v_r \partial v_t} \\ &+ \frac{\partial^2 v_t}{\partial v_1^2} \frac{\partial g}{\partial v_t} + \left(\frac{\partial v_t}{\partial v_1}\right)^2 \frac{\partial^2 g}{\partial v_t^2} + \frac{\partial v_t}{\partial v_1} \frac{\partial v_r}{\partial v_1} \frac{\partial^2 g}{\partial v_t \partial v_r}, \end{aligned} \quad (\text{A5})$$

where the derivatives $\partial^2 g/\partial v_2^2$ and $\partial^2 g/\partial v_3^2$ are obtained by direct replacements. In equation (A5), the only non-zero second-order ve-

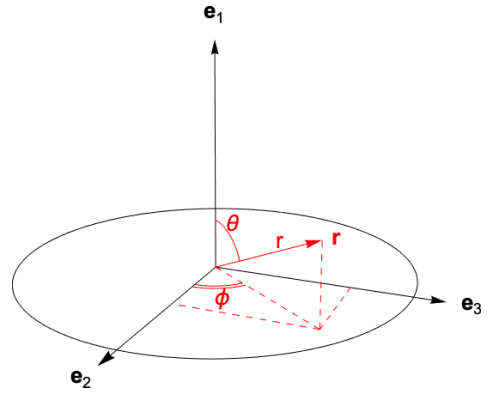


Figure A1. Arbitrary frame used to describe the test particle’s position, as in equation (A1).

locity gradients follow once again from equation (A2) and read

$$\frac{\partial^2 v_t}{\partial v_1^2} = \frac{\cos \theta}{v_t} \left(\sin^2 \theta - \frac{(v_1 - v_r \cos \theta)^2}{v_t^2} \right), \quad (\text{A6a})$$

$$\frac{\partial^2 v_t}{\partial v_2^2} = \frac{1}{v_t} \left((1 - \sin^2 \theta \cos^2 \phi) - \frac{(v_2 - v_r \sin \theta \cos \phi)^2}{v_t^2} \right), \quad (\text{A6b})$$

$$\frac{\partial^2 v_t}{\partial v_3^2} = \frac{1}{v_t} \left((1 - \sin^2 \theta \sin^2 \phi) - \frac{(v_3 - v_r \sin \theta \sin \phi)^2}{v_t^2} \right). \quad (\text{A6c})$$

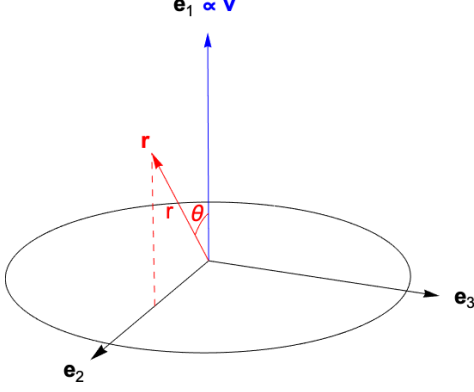


Figure A2. Tailored frame used to compute the parallel and perpendicular local velocity deflections in equation (A9).

A2 Special frame

Having obtained generic expressions for the needed gradients, we can now evaluate them in an appropriate frame. More precisely, as illustrated in Fig. A2, we consider the particular frame $\mathbf{e}_1 = \hat{v}$ and $\phi = 0$. In that frame, the velocities simply reduce to $v_1 = v$, $v_2 = v_3 = 0$. Similarly, we also have $\cos \theta = v_r/v$, and $\sin \theta = v_t/v$.

Benefiting from these simple relations, we can now use equations (A3) and (A4) to get a simple expression for the first-order gradient of h as

$$\frac{\partial h}{\partial v_1} = \frac{v_r}{v} \frac{\partial h}{\partial v_r} + \frac{v_t}{v} \frac{\partial h}{\partial v_t}, \quad (\text{A7})$$

Similarly, using equations (A5) and (A6), we also obtain a simple expression for the needed second-order gradients of g via

$$\frac{\partial^2 g}{\partial v_1^2} = \left(\frac{v_r}{v}\right)^2 \frac{\partial^2 g}{\partial v_r^2} + \frac{2v_r v_t}{v^2} \frac{\partial^2 g}{\partial v_t \partial v_r} + \left(\frac{v_t}{v}\right)^2 \frac{\partial^2 g}{\partial v_t^2}, \quad (\text{A8a})$$

$$\frac{\partial^2 g}{\partial v_2^2} = \left(\frac{v_t}{v}\right)^2 \frac{\partial^2 g}{\partial v_r^2} - \frac{2v_r v_t}{v^2} \frac{\partial^2 g}{\partial v_t \partial v_r} + \left(\frac{v_r}{v}\right)^2 \frac{\partial^2 g}{\partial v_t^2}, \quad (\text{A8b})$$

$$\frac{\partial^2 g}{\partial v_3^2} = \frac{1}{v_t} \frac{\partial g}{\partial v_t}. \quad (\text{A8c})$$

In the particular frame from Fig. A2, one has $\Delta v_1 = \Delta v_{\parallel}$ and $\Delta v_2^2 + \Delta v_3^2 = \Delta v_{\perp}^2$, with Δv_{\parallel} and Δv_{\perp} the velocity deflections parallel and perpendicular to the star's motion. This translates into the local velocity diffusion coefficients

$$\langle \Delta v_{\parallel} \rangle = \langle \Delta v_1 \rangle, \quad (\text{A9a})$$

$$\langle (\Delta v_{\parallel})^2 \rangle = \langle (\Delta v_1)^2 \rangle, \quad (\text{A9b})$$

$$\langle (\Delta v_{\perp})^2 \rangle = \langle (\Delta v_2)^2 \rangle + \langle (\Delta v_3)^2 \rangle. \quad (\text{A9c})$$

The final step of the calculation is then to inject the expressions of the gradients from equations (A7) and (A8) into equation (1). Overall, this leads to the final result from equation (3).

One could fear that equation (3) presents singularities for $v = 0$ and $v_t = 0$. Fortunately, those are only coordinate singularities. Indeed the limiting case $v = 0$ only occurs at pericentre and apocentre of radial orbits, i.e. orbits with $v_t = 0$. In that limit, one has $v = v_r$, so that $v_r/v = 1$ and $v_t/v = 0$, resolving the $1/v$ singularities in equation (3). As for the $1/v_t$ singularity, we note that $\partial g / \partial v_t$ vanishes in $v_t = 0$ – as shown in §C2 – so that $\lim_{v_t \rightarrow 0} (\partial g / \partial v_t) / v_t = \partial^2 g / \partial v_t^2$. This ensures similarly that there are no $1/v_t$ singularities in equation (3).

APPENDIX B: ISOTROPIC DIFFUSION COEFFICIENTS

The anisotropic diffusion coefficients from equation (3) must reduce to the known isotropic expressions in the limit of an isotropic DF, $F_{\text{tot}} = F_{\text{tot}}(E)$. We check it in this Appendix.

Assuming that the cluster is isotropic, we generically have $h(v_r, v_t) = h(v)$ with $v^2 = v_r^2 + v_t^2$ and similarly for $g(v_r, v_t) = g(v)$. Focusing back on equation (3), we can rewrite the derivatives appearing in $\langle \Delta v_{\parallel} \rangle$ as

$$\frac{\partial h}{\partial v_r} = \frac{v_r}{v} \frac{\partial h}{\partial v}, \quad \frac{\partial h}{\partial v_t} = \frac{v_t}{v} \frac{\partial h}{\partial v}. \quad (\text{B1})$$

As required by equation (3), we obtain

$$\frac{v_r}{v} \frac{\partial h}{\partial v_r} + \frac{v_t}{v} \frac{\partial h}{\partial v_t} = \frac{\partial h}{\partial v}. \quad (\text{B2})$$

Similarly, the derivatives involved in $\langle (\Delta v_{\parallel})^2 \rangle$ and $\langle (\Delta v_{\perp})^2 \rangle$ in equation (3) generically read

$$\frac{\partial^2 g}{\partial v_r^2} = \frac{\partial}{\partial v_r} \left(\frac{\partial v}{\partial v_r} \frac{\partial g}{\partial v}(v) \right) = \frac{v_r^2}{v^3} \frac{\partial g}{\partial v} + \frac{v_r^2}{v^2} \frac{\partial^2 g}{\partial v^2}, \quad (\text{B3a})$$

$$\frac{\partial^2 g}{\partial v_t \partial v_r} = \frac{\partial}{\partial v_t} \left(\frac{\partial v}{\partial v_r} \frac{\partial g}{\partial v}(v) \right) = -\frac{v_r v_t}{v^3} \frac{\partial g}{\partial v} + \frac{v_r v_t}{v^2} \frac{\partial^2 g}{\partial v^2}, \quad (\text{B3b})$$

$$\frac{\partial^2 g}{\partial v_t^2} = \frac{\partial}{\partial v_t} \left(\frac{v_t}{v} \frac{\partial g}{\partial v}(v) \right) = \frac{v_r^2}{v^3} \frac{\partial g}{\partial v} + \frac{v_t^2}{v^2} \frac{\partial^2 g}{\partial v^2}, \quad (\text{B3c})$$

$$\frac{\partial g}{\partial v_t} = \frac{\partial v}{\partial v_t} \frac{\partial g}{\partial v}(v) = \frac{v_t}{v} \frac{\partial g}{\partial v}. \quad (\text{B3d})$$

Therefore, in the isotropic limit, we obtain the simplifications

$$\left(\frac{v_t}{v}\right)^2 \frac{\partial^2 g}{\partial v_r^2} + \frac{2v_r v_t}{v^2} \frac{\partial^2 g}{\partial v_t \partial v_r} + \left(\frac{v_r}{v}\right)^2 \frac{\partial^2 g}{\partial v_t^2} = \frac{\partial^2 g}{\partial v^2}, \quad (\text{B4a})$$

$$\left(\frac{v_t}{v}\right)^2 \frac{\partial^2 g}{\partial v_r^2} - \frac{2v_r v_t}{v^2} \frac{\partial^2 g}{\partial v_t \partial v_r} + \left(\frac{v_r}{v}\right)^2 \frac{\partial^2 g}{\partial v_t^2} + \frac{1}{v_t} \frac{\partial g}{\partial v_t} = \frac{2}{v} \frac{\partial g}{\partial v}. \quad (\text{B4b})$$

Finally, plugging equations (B2) and (B4) into the local velocity diffusion coefficients from equation (3) yields the local isotropic diffusion coefficients (Binney & Tremaine 2008, equation L.25)

$$\langle \Delta v_{\parallel} \rangle = 4\pi G^2 (m + m_b) \ln \Lambda \frac{\partial h}{\partial v}, \quad (\text{B5a})$$

$$\langle (\Delta v_{\parallel})^2 \rangle = 4\pi G^2 m_b \ln \Lambda \frac{\partial^2 g}{\partial v^2}, \quad (\text{B5b})$$

$$\langle (\Delta v_{\perp})^2 \rangle = \frac{8\pi G^2 m_b \ln \Lambda}{v} \frac{\partial g}{\partial v}. \quad (\text{B5c})$$

In practice, the derivatives from equation (B5) can be evaluated via

$$\frac{\partial h}{\partial v} = -\frac{4\pi}{v} K_1(r, v), \quad (\text{B6a})$$

$$\frac{\partial g}{\partial v} = \frac{8\pi v}{3} \left(2K_0(r, v) + 3K_1(r, v) - K_3(r, v) \right), \quad (\text{B6b})$$

$$\frac{\partial^2 g}{\partial v^2} = \frac{8\pi}{3} \left(K_0(r, v) + K_3(r, v) \right), \quad (\text{B6c})$$

where we defined the integrals

$$K_0(r, v) = \int_v^{+\infty} dv' v' F_{\text{tot}}(r, v'), \quad (\text{B7a})$$

$$K_1(r, v) = \int_0^v dv' v' \left(\frac{v'}{v} \right) F_{\text{tot}}(r, v'), \quad (\text{B7b})$$

$$K_3(r, v) = \int_0^v dv' v' \left(\frac{v'}{v} \right)^3 F_{\text{tot}}(r, v'). \quad (\text{B7c})$$

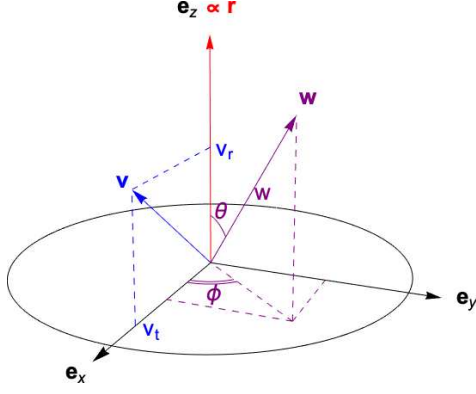


Figure C1. Tailored frame used to compute $h(r, v_r, v_t)$ and $g(r, v_r, v_t)$ as in equation (C1).

APPENDIX C: GRADIENTS OF POTENTIALS

In equation (3), we obtained a generic expression of the anisotropic diffusion coefficients as functions of the gradients of the Rosenbluth potentials with respect to (v_r, v_t) . In this Appendix, we obtain explicit expressions for the needed gradients as simple non-singular three-dimensional integrals over velocity space.

C1 Derivation of gradient expressions

The Rosenbluth potentials, h and g , are generically given by equation (2). Our goal is to pick an appropriate frame to express them as $h(r, v_r, v_t)$ and $g(r, v_r, v_t)$, so as to compute their gradients with respect to v_r and v_t .

Following Fig. C1, we now fix our frame to be $\mathbf{e}_z = \hat{r}$ and $\mathbf{e}_x = \mathbf{v}_t/v_t$. In that frame, the velocity of the test particle is simply $v_x = v_t, v_y = 0, v_z = v_r$. In the same frame, we can decompose the velocity difference $\mathbf{w} = \mathbf{v} - \mathbf{v}'$ as

$$w_x = w \sin \theta \cos \phi, \quad w_y = w \sin \theta \sin \phi, \quad w_z = w \cos \theta. \quad (\text{C1})$$

As a consequence, the velocity of the background particle, $\mathbf{v}' = \mathbf{v} - \mathbf{w}$ reads

$$v'_x = v_t - w \sin \theta \cos \phi, \quad v'_y = -w \sin \theta \sin \phi, \quad v'_z = v_r - w \cos \theta, \quad (\text{C2})$$

with the associated radial and tangential velocity decomposition

$$v'_r = v_r - w \cos \theta, \quad (\text{C3a})$$

$$v'_t = \sqrt{(v_t - w \sin \theta \cos \phi)^2 + (w \sin \theta \sin \phi)^2}. \quad (\text{C3b})$$

The energy and angular momentum (E', L') of the background particle are then naturally given by

$$E' = \psi(r) + \frac{1}{2}v_r'^2 + \frac{1}{2}v_t'^2, \quad L' = rv_t'. \quad (\text{C4})$$

Within that same frame, the Rosenbluth potentials from equation (C1) read

$$h(\mathbf{r}, \mathbf{v}) = \int d\mathbf{w} d\theta d\phi w \sin \theta F_{\text{tot}}(r, \mathbf{v} - \mathbf{w}), \quad (\text{C5a})$$

$$g(\mathbf{r}, \mathbf{v}) = \int d\mathbf{w} d\theta d\phi w^3 \sin \theta F_{\text{tot}}(r, \mathbf{v} - \mathbf{w}). \quad (\text{C5b})$$

We are now in a position to compute the needed gradients of the Rosenbluth potentials present in equation (3). Starting from equa-

tion (2), we must compute

$$\frac{\partial h}{\partial v_r} = \int d\mathbf{v}' F_{\text{tot}}(r, \mathbf{v}') \frac{\partial}{\partial v_r} \left(\frac{1}{|\mathbf{v} - \mathbf{v}'|} \right), \quad (\text{C6a})$$

$$\frac{\partial h}{\partial v_t} = \int d\mathbf{v}' F_{\text{tot}}(r, \mathbf{v}') \frac{\partial}{\partial v_t} \left(\frac{1}{|\mathbf{v} - \mathbf{v}'|} \right). \quad (\text{C6b})$$

Here, we have $|\mathbf{v} - \mathbf{v}'|^2 = w_x^2 + w_y^2 + w_z^2$ with

$$w_x = v_t - v'_x, \quad w_y = -v'_y, \quad w_z = v_r - v'_z, \quad (\text{C7})$$

so that the radial and tangential derivative in equation (C6) can be computed as

$$\frac{\partial h}{\partial v_r} = \int d\mathbf{v}' F_{\text{tot}}(r, \mathbf{v}') \frac{-(v_r - v'_z)}{|\mathbf{v} - \mathbf{v}'|^3}, \quad (\text{C8a})$$

$$\frac{\partial h}{\partial v_t} = \int d\mathbf{v}' F_{\text{tot}}(r, \mathbf{v}') \frac{-(v_t - v'_x)}{|\mathbf{v} - \mathbf{v}'|^3}. \quad (\text{C8b})$$

The last step of the calculation is to perform the change of integration variables $\mathbf{v}' \rightarrow \mathbf{w}$, and use equations (C1) and (C7). We obtain

$$\frac{\partial h}{\partial v_r} = - \int d\mathbf{w} d\theta d\phi \sin \theta \cos \theta F_{\text{tot}}(r, \mathbf{v} - \mathbf{w}), \quad (\text{C9a})$$

$$\frac{\partial h}{\partial v_t} = - \int d\mathbf{w} d\theta d\phi \sin^2 \theta \cos \phi F_{\text{tot}}(r, \mathbf{v} - \mathbf{w}). \quad (\text{C9b})$$

The same method can be applied for the gradients of $g(r, v_r, v_t)$. Starting from equation (2), similarly to equation (C8), we obtain

$$\frac{\partial g}{\partial v_r} = \int d\mathbf{v}' F_{\text{tot}}(r, \mathbf{v}') \frac{v_r - v'_z}{|\mathbf{v} - \mathbf{v}'|^3}, \quad (\text{C10a})$$

$$\frac{\partial g}{\partial v_t} = \int d\mathbf{v}' F_{\text{tot}}(r, \mathbf{v}') \frac{v_t - v'_x}{|\mathbf{v} - \mathbf{v}'|^3}. \quad (\text{C10b})$$

Following the same step as in (C9), this becomes

$$\frac{\partial g}{\partial v_r} = \int d\mathbf{w} d\theta d\phi w^2 \sin \theta \cos \theta F_{\text{tot}}(r, \mathbf{v} - \mathbf{w}), \quad (\text{C11a})$$

$$\frac{\partial g}{\partial v_t} = \int d\mathbf{w} d\theta d\phi w^2 \sin^2 \theta \cos \phi F_{\text{tot}}(r, \mathbf{v} - \mathbf{w}). \quad (\text{C11b})$$

To compute the second-order gradients of g , we differentiate equation (C10) once more to get

$$\frac{\partial^2 g}{\partial v_r^2} = h - \int d\mathbf{v}' F_{\text{tot}}(r, \mathbf{v}') \frac{(v_r - v'_z)^2}{|\mathbf{v} - \mathbf{v}'|^3}, \quad (\text{C12a})$$

$$\frac{\partial^2 g}{\partial v_t \partial v_r} = - \int d\mathbf{v}' F_{\text{tot}}(r, \mathbf{v}') \frac{(v_r - v'_z)(v_t - v'_x)}{|\mathbf{v} - \mathbf{v}'|^3}, \quad (\text{C12b})$$

$$\frac{\partial^2 g}{\partial v_t^2} = h - \int d\mathbf{v}' F_{\text{tot}}(r, \mathbf{v}') \frac{(v_t - v'_x)^2}{|\mathbf{v} - \mathbf{v}'|^3}. \quad (\text{C12c})$$

Using once again the spherical coordinates from Fig. C1, this gives

$$\frac{\partial^2 g}{\partial v_r^2} = h - \int d\mathbf{w} d\theta d\phi w \sin \theta \cos^2 \theta F_{\text{tot}}(r, \mathbf{v} - \mathbf{w}), \quad (\text{C13a})$$

$$\frac{\partial^2 g}{\partial v_t \partial v_r} = - \int d\mathbf{w} d\theta d\phi w \sin^2 \theta \cos \theta \cos \phi F_{\text{tot}}(r, \mathbf{v} - \mathbf{w}), \quad (\text{C13b})$$

$$\frac{\partial^2 g}{\partial v_t^2} = h - \int d\mathbf{w} d\theta d\phi w \sin^3 \theta \cos^2 \phi F_{\text{tot}}(r, \mathbf{v} - \mathbf{w}), \quad (\text{C13c})$$

where the value of $h(r, v_r, v_t)$ follows from equation (C5).

Equations (C5)–(C13) are the main results of this Appendix. We emphasise that these expressions do not involve any diverging velocity denominators, nor any gradients of the cluster's DF, F_{tot} .

C2 Symmetries

Focusing again on equations (C3) and (C4), we find that E' and L' are left unchanged by the transformation $(v_r, \theta) \rightarrow (-v_r, \pi - \theta)$. As a consequence, we get from equation (C5) that h and g are both even functions in v_r . From the same equations (C3) and (C4), we also get that for $v_t = 0$, E' and L' are independent of ϕ . When used in equation (C5) to perform the obvious integral over ϕ , this imposes that $\partial g / \partial v_t$ vanishes for $v_t = 0$.

C3 Integration strategy

In equations (C5)–(C13), the integration bounds are naturally set by the constraints $0 \leq w < +\infty$, $0 \leq \theta \leq \pi$, and $0 \leq \phi \leq 2\pi$. This integration domain may be further constrained by using the fact that the DF $F_{\text{tot}}(r, \mathbf{v} - \mathbf{w}) = F_{\text{tot}}(E', L')$ in the integrand is non-zero only for bound perturbing orbits.

Expanding equation (C4) yields

$$\begin{aligned} E' &= \psi(r) + \frac{1}{2}(v^2 + w^2) - w(v_r \cos \theta + v_t \sin \theta \cos \phi) \\ &= \frac{1}{2}w^2 - w(v_r \cos \theta + v_t \sin \theta \cos \phi) + E, \end{aligned} \quad (\text{C14})$$

where we introduced $E = \psi(r) + \frac{1}{2}v^2$ the test star's energy. We now want to restrain our integration domain to $E' < 0$, i.e. to bound perturbing orbits. At fixed (θ, ϕ) , the r.h.s of equation (C14) is a polynomial in w with positive leading coefficient. This polynomial is therefore always positive if it has no root, or only negative between its roots if it has some. Its discriminant is

$$\Delta = (v_r \cos \theta + v_t \sin \theta \cos \phi)^2 - 2E. \quad (\text{C15})$$

In practice, we evaluate diffusion coefficients only for bound test stars, i.e. test stars satisfying $E < 0$, from which we get $\Delta > 0$. The two roots of the polynomial are given by

$$w_+ = v_r \cos \theta + v_t \sin \theta \cos \phi + \sqrt{\Delta} > 0, \quad (\text{C16a})$$

$$w_- = v_r \cos \theta + v_t \sin \theta \cos \phi - \sqrt{\Delta} < 0. \quad (\text{C16b})$$

As a consequence, we fix our integration domains to $0 \leq \theta \leq \pi$, $0 \leq \phi \leq 2\pi$, and $0 \leq w \leq w_+(\theta, \phi)$. In practice, the whole integration is performed using the standard midpoint rule within each of the respective allowed domains. We typically use $N_K = 10^2$ sampling nodes for the computations presented throughout the main text (see also Fig. D1).

APPENDIX D: COEFFICIENTS FROM LANDAU

The local diffusion coefficients presented in equation (1) are expressed as a function of the Rosenbluth potentials. The same diffusion coefficients can also be obtained from the homogeneous Landau equation (see Chavanis 2013b, for a review). In this Appendix, we start from this equivalent writing to check our calculations and numerical implementations.

Starting from equations (F.3)–(F.6) in Chavanis (2013b), we consider the local diffusion coefficients

$$\langle \Delta v_i \rangle = \frac{1}{2}(2\pi)^4 (m + m_b) \int d\mathbf{v}' d\mathbf{k} k_i k_j \delta_D(\mathbf{k} \cdot \mathbf{w}) \hat{u}(k)^2 \frac{\partial F_{\text{tot}}}{\partial v_j'}, \quad (\text{D1a})$$

$$\langle \Delta v_i \Delta v_j \rangle = (2\pi)^4 m_b \int d\mathbf{v}' d\mathbf{k} k_i k_j \delta_D(\mathbf{k} \cdot \mathbf{w}) \hat{u}(k)^2 F_{\text{tot}}, \quad (\text{D1b})$$

with $\mathbf{w} = \mathbf{v} - \mathbf{v}'$ standing for the velocity difference between the test and background particles. In that expression, we also introduced $(2\pi)^3 \hat{u}(k) = -4\pi G/k^2$ as the Fourier transform of the

gravitational potential, while the DF, F_{tot} , and its derivatives are evaluated at $(\mathbf{r}, \mathbf{v}')$.

Our goal is now to further simplify equation (D1) by using the same frame as in Fig. A2. We first introduce spherical coordinates (k, θ_k, ϕ_k) to write the radial frequency, \mathbf{k} , as

$$k_1 = k \cos \theta_k, \quad k_2 = k \sin \theta_k \cos \phi_k, \quad k_3 = k \sin \theta_k \sin \phi_k. \quad (\text{D2})$$

In order to make progress with equation (D1), we must deal with the resonance condition $\delta_D(\mathbf{k} \cdot \mathbf{w})$. With the present frame, it imposes the cancellation of

$$\mathbf{k} \cdot \mathbf{w} = k(v - v'_1) \cos \theta_k - k \sin \theta_k (v'_2 \cos \phi_k + v'_3 \sin \phi_k). \quad (\text{D3})$$

We note that $\mathbf{k} \cdot \mathbf{w}$ is generically a monotonic function of v'_i when varied individually. As such, if one decides to solve the resonance condition with respect to a given v'_i , one can use the relation

$$\delta_D(\mathbf{k} \cdot \mathbf{w}) = \frac{\delta_D(v'_i - v'_{i,\text{res}})}{|\partial(\mathbf{k} \cdot \mathbf{w}) / \partial v'_i|_{v'_i = v'_{i,\text{res}}}}, \quad (\text{D4})$$

where $v'_{i,\text{res}}$ stands for the (single) root of the function $v'_{i,\text{res}} \mapsto \mathbf{k} \cdot \mathbf{w}$. From equation (D3), we generically find that, depending on the considered coordinate, the resonance condition can generically be solved as

$$v'_{1,\text{res}} = v - \tan \theta_k (v'_2 \cos \phi_k + v'_3 \sin \phi_k), \quad (\text{D5a})$$

$$v'_{2,\text{res}} = \frac{(v - v'_1) \cot \theta_k - v'_3 \sin \phi_k}{\cos \phi_k}, \quad (\text{D5b})$$

$$v'_{3,\text{res}} = \frac{(v - v'_1) \cot \theta_k - v'_2 \cos \phi_k}{\sin \phi_k}, \quad (\text{D5c})$$

with the associated gradients

$$\frac{\partial(\mathbf{k} \cdot \mathbf{w})}{\partial v'_1} = -k \cos \theta_k, \quad (\text{D6a})$$

$$\frac{\partial(\mathbf{k} \cdot \mathbf{w})}{\partial v'_2} = -k \sin \theta_k \cos \phi_k, \quad (\text{D6b})$$

$$\frac{\partial(\mathbf{k} \cdot \mathbf{w})}{\partial v'_3} = -k \sin \theta_k \sin \phi_k. \quad (\text{D6c})$$

Let us now illustrate the calculation of $\langle (\Delta v_1)^2 \rangle$. Starting from equation (D1), we write

$$\begin{aligned} \langle (\Delta v_1)^2 \rangle &= (2\pi)^4 m_b \int d\mathbf{v}' d\mathbf{k} k_1^2 \delta_D(\mathbf{k} \cdot \mathbf{w}) \hat{u}(k)^2 F_{\text{tot}} \\ &= 4m_b G^2 \int d\mathbf{v}' dk d\theta_k d\phi_k \sin \theta_k \cos^2 \theta_k \delta_D(\mathbf{k} \cdot \mathbf{w}) F_{\text{tot}}. \end{aligned} \quad (\text{D7})$$

Following equation (D4), we use v'_1 to solve the resonance condition and obtain

$$\begin{aligned} \langle (\Delta v_1)^2 \rangle &= 4m_b G^2 \int d\mathbf{v}' dk d\theta_k d\phi_k \frac{\sin \theta_k \cos^2 \theta_k}{|k \cos \theta_k|} \delta_D(v'_1 - v'_{1,\text{res}}) F_{\text{tot}} \\ &= 4m_b G^2 \int d\mathbf{v}' \frac{dk}{k} d\theta_k d\phi_k \sin \theta_k |\cos \theta_k| \delta_D(v'_1 - v'_{1,\text{res}}) F_{\text{tot}}. \end{aligned} \quad (\text{D8})$$

Importantly, we emphasise that using here v'_1 to solve the resonance condition naturally leads to the simplification of any diverging denominators. As expected, we must heuristically cure the integral over radial frequency on both small and large scales (see, e.g., §2.6 in Chavanis 2013b). Introducing the Coulomb logarithm

$$\ln \Lambda = \int_{k_{\text{min}}}^{k_{\text{max}}} dk/k = \ln(k_{\text{max}}/k_{\text{min}}), \quad (\text{D9})$$

equation (D8) finally becomes

$$\langle (\Delta v_{\parallel})^2 \rangle = A m_b \int_{v'_1=v'_{1,\text{res}}} dv'_2 dv'_3 d\theta_k d\phi_k \sin \theta_k |\cos \theta_k| F_{\text{tot}}, \quad (\text{D10})$$

with $A = 4G^2 \ln \Lambda$ and $F_{\text{tot}} = F_{\text{tot}}(\mathbf{r}, \mathbf{v}')$. In that expression, the subscript $v'_1 = v'_{1,\text{res}}$ attached to the integral symbol implies that the resonance condition from equation (D5) has been applied to the variable v'_1 .

Following equation (A9), we can use the exact same approach to compute the parallel and perpendicular diffusion coefficients. During that calculation, we pay attention to solving the resonance condition $\delta_D(\mathbf{k} \cdot \mathbf{w})$ with respect to the appropriate velocity, v'_i , to ensure that the diverging denominators naturally cancel out. Overall, one gets

$$\langle \Delta v_{\parallel} \rangle = A \frac{1}{2} (m + m_b) \quad (\text{D11a})$$

$$\times \left[\int_{v'_1=v'_{1,\text{res}}} dv'_2 dv'_3 d\theta_k d\phi_k |\cos \theta_k| \sin \theta_k \frac{\partial F_{\text{tot}}}{\partial v'_1} \right. \\ \left. + \int_{v'_2=v'_{2,\text{res}}} dv'_1 dv'_3 d\theta_k d\phi_k \cos \theta_k \sin \theta_k \text{sgn}(\cos \phi_k) \frac{\partial F_{\text{tot}}}{\partial v'_2} \right. \\ \left. + \int_{v'_3=v'_{3,\text{res}}} dv'_1 dv'_2 d\theta_k d\phi_k \cos \theta_k \sin \theta_k \text{sgn}(\sin \phi_k) \frac{\partial F_{\text{tot}}}{\partial v'_3} \right],$$

$$\langle (\Delta v_{\parallel})^2 \rangle = A m_b \int_{v'_1=v'_{1,\text{res}}} dv'_2 dv'_3 d\theta_k d\phi_k |\cos \theta_k| \sin \theta_k F_{\text{tot}}, \quad (\text{D11b})$$

$$\langle (\Delta v_{\perp})^2 \rangle = A m_b \left[\int_{v'_2=v'_{2,\text{res}}} dv'_1 dv'_3 d\theta_k d\phi_k \sin^2 \theta_k |\cos \phi_k| F_{\text{tot}} \quad (\text{D11c}) \right. \\ \left. + \int_{v'_3=v'_{3,\text{res}}} dv'_1 dv'_2 d\theta_k d\phi_k \sin^2 \theta_k |\sin \phi_k| F_{\text{tot}} \right],$$

with $\text{sgn}(x) = x/|x|$.

The integration domains in equation (D11) are respectively given by $0 \leq \theta_k \leq \pi$ and $0 \leq \phi_k \leq 2\pi$ for the angular variables, and $-\sqrt{-2\psi(r)} \leq v'_i \leq \sqrt{-2\psi(r)}$ for the velocity ones. In equation (D11), the DF and its derivatives are evaluated in (r, \mathbf{v}') , or equivalently in (E', L') given by

$$E' = \psi(r) + \frac{1}{2} v'^2, \quad L' = r v'_t, \quad (\text{D12a})$$

$$v'_r = \frac{v'_1 v_r}{v} + \frac{v'_2 v_t}{v}, \quad v'_t = \sqrt{v'^2 - v_r'^2}, \quad v'^2 = v_1'^2 + v_2'^2 + v_3'^2. \quad (\text{D12b})$$

Furthermore, all the derivatives of $F_{\text{tot}} = F_{\text{tot}}(E', L')$ with respect to v'_i are computed using the chain rule so that

$$\frac{\partial F_{\text{tot}}}{\partial v'_i} = \frac{\partial E'}{\partial v'_i} \frac{\partial F_{\text{tot}}}{\partial E'} + \frac{\partial L'}{\partial v'_i} \frac{\partial F_{\text{tot}}}{\partial L'}, \quad (\text{D13})$$

where, following Fig. A2 and equation (C4), the remaining gradients simply read

$$\frac{\partial E'}{\partial v'_i} = v'_i, \quad \frac{\partial L'}{\partial v'_i} = r \left(\frac{v'_i}{v'_t} - \frac{v'_r}{v'_t} \frac{\partial v'_r}{\partial v'_i} \right), \quad (\text{D14a})$$

$$\frac{\partial v'_r}{\partial v'_i} = \begin{cases} v_r/v, & \text{if } i = 1, \\ v_t/v, & \text{if } i = 2, \\ 0, & \text{if } i = 3. \end{cases} \quad (\text{D14b})$$

Equation (D11) is the main result of this Appendix. It captures the exact same velocity diffusion coefficients as equation (3) from the main text. Yet, these expressions require the computation of four-dimensional integrals, and involve derivatives of the cluster's DF. These two difficulties are lifted by using Rosenbluth's approach as the final expressions of the potentials only involve three-

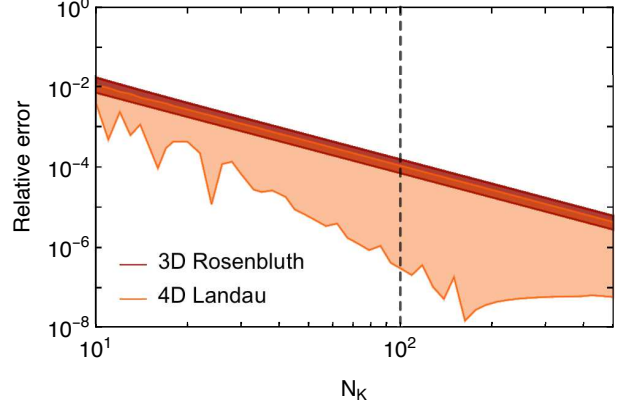


Figure D1. Relative errors in $\langle (\Delta v_{\parallel})^2 \rangle(r, v_r, v_t)$ as computed via the Rosenbluth expressions (equation 3) or the Landau expressions (equation D11). Both expressions are computed using a midpoint sampling with N_K nodes. Relative errors are computed with respect to the Rosenbluth expressions using $N_K = 5000$. The level lines correspond to the 16% and 84% centiles over 160 values of (r, v_r, v_t) drawn uniformly within $0 \leq r \leq b$, $0 \leq v_r \leq \sqrt{-2\psi(r)}$ and $0 \leq v_t \leq \sqrt{-2\psi(r) - v_r^2}$. Both approaches are found to be in agreement.

dimensional integrals without any occurrences of derivatives of the cluster's DF, see equations (C5)–(C13).

In Fig. D1, we illustrate the relative error between the Rosenbluth expressions (equation 3) and the Landau ones (equation D11), as a function of the number of nodes, N_K , used in the midpoint rule. Reassuringly, we find that (i) both expressions are in agreement; (ii) the use of the midpoint rule ensures a convergence in $O(N_K^{-2})$. In practice, we used $N_K = 10^2$ sampling nodes in the main text, ensuring a relative error of the order of 10^{-4} .

APPENDIX E: DISTRIBUTION FUNCTION

To investigate the effects associated with velocity anisotropies, we consider the families of DFs put forward by Dejonghe (1987)

$$F_{\text{tot}}(E, L; q) = \frac{M}{L_0^3} \frac{3 \Gamma(6-q) \tilde{E}^{\gamma/2-q}}{2(2\pi)^{5/2}} \mathbb{H}_q \left(\frac{\tilde{L}^2}{2\tilde{E}} \right), \quad (\text{E1})$$

where q controls the flavour and degree of anisotropy in the cluster (see Fig. 1). In equation (E1), we introduced the rescaled energy and angular momentum, $\tilde{E} = E/E_0$ and $\tilde{L} = L/L_0$, with

$$E_0 = -GM/b, \quad L_0 = \sqrt{GMb}. \quad (\text{E2})$$

We also introduced the function

$$\mathbb{H}_q(x) = \begin{cases} \frac{{}_2F_1(\frac{1}{2}q, q - \frac{7}{2}, 1; x)}{\Gamma(\frac{9}{2} - q)}, & \text{if } x \leq 1, \\ \frac{{}_2F_1(\frac{1}{2}q, \frac{1}{2}q, \frac{1}{2}(9-q); 1/x)}{\Gamma(1 - \frac{1}{2}q)\Gamma(\frac{1}{2}(9-q))} \frac{1}{x^{q/2}}, & \text{if } x \geq 1, \end{cases} \quad (\text{E3})$$

with ${}_2F_1$ the hypergeometric function and Γ the Gamma function. In Fig. E1, we illustrate the reduced DF, $F = 2LF_{\text{tot}}$ (see equation 5), in action space for various anisotropies.

APPENDIX F: ORBIT-AVERAGING

In order to orbit-average the local diffusion coefficients, we proceed in three steps: (i) we compute the local diffusion coefficients in the

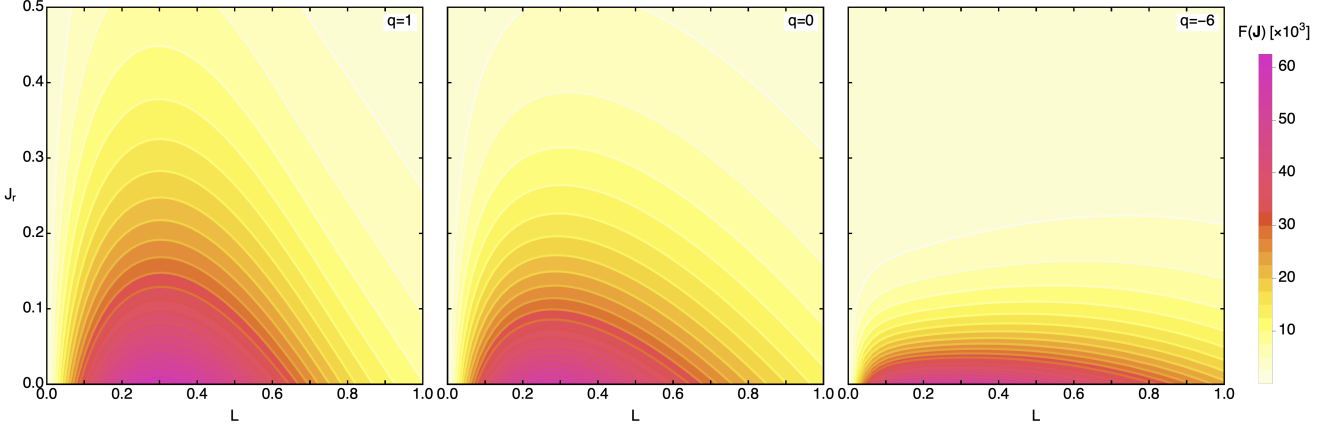


Figure E1. Illustration of the reduced DF from equation (E1) for a radially anisotropic distribution ($q = 1$, left), an isotropic one ($q = 0$, middle), and a tangentially anisotropic one ($q = -6$, right). The radially (resp. tangentially) anisotropic DF shows a higher concentration of radial (resp. tangential) orbits, i.e. orbits with small L (resp. small J_r).

orbit's invariants E and L ; (ii) we carry out the orbit average using an explicit effective anomaly which regularises the process; (iii) we compute the corresponding orbit-averaged diffusion coefficients in terms of the actions, J_r and L .

F1 From velocity to energy and angular momentum

Equation (3) gives the local velocity diffusion coefficients. Following equation (C15)–(C19) of Bar-Or & Alexander (2016), these can be translated into local diffusion coefficients in energy and angular momentum via

$$\langle \Delta E \rangle = \frac{1}{2} \langle (\Delta v_{\parallel})^2 \rangle + \frac{1}{2} \langle (\Delta v_{\perp})^2 \rangle + v \langle \Delta v_{\parallel} \rangle, \quad (\text{F1a})$$

$$\langle (\Delta E)^2 \rangle = v^2 \langle (\Delta v_{\parallel})^2 \rangle, \quad (\text{F1b})$$

$$\langle \Delta L \rangle = \frac{L}{v} \langle \Delta v_{\parallel} \rangle + \frac{1}{4} \frac{r^2}{L} \langle (\Delta v_{\perp})^2 \rangle, \quad (\text{F1c})$$

$$\langle (\Delta L)^2 \rangle = \frac{L^2}{v^2} \langle (\Delta v_{\parallel})^2 \rangle + \frac{1}{2} (r^2 - (L/v)^2) \langle (\Delta v_{\perp})^2 \rangle, \quad (\text{F1d})$$

$$\langle \Delta E \Delta L \rangle = L \langle (\Delta v_{\parallel})^2 \rangle. \quad (\text{F1e})$$

To evaluate equation (F1), we must switch between (r, v_r, v_t) and (E, L) . This is naturally done through

$$E = \psi(r) + \frac{1}{2} v_r^2 + \frac{1}{2} v_t^2, \quad L = r v_t, \quad (\text{F2})$$

and the associated inverse transformation

$$v_r = \pm \sqrt{2(E - \psi(r)) - L^2/r^2}, \quad v_t = L/r. \quad (\text{F3})$$

In equation (F3), the “+” case for v_r corresponds to the outward radial motion from pericentre to apocentre, while the “−” case corresponds to the inward motion. In practice, as the Rosenbluth potentials h and g are even in v_r (see §C2), we can safely limit ourselves to the outward part of the orbit, i.e. $v_r > 0$, when orbit-averaging.

F2 Plummer effective anomaly

Once the local diffusion coefficients in (E, L) estimated, they must be averaged along the test star's orbit, as in equation (4). Following Hénon (1971), we perform the orbit-average with respect to an effective anomaly $-1 \leq u \leq 1$, such that $r(u = -1) = r_p$ and

$r(u = 1) = r_a$. Limiting ourselves to the outward part of the orbit, we rewrite equation (4) as

$$D_E = \frac{2}{T} \int_{-1}^1 du \Theta(u) \langle \Delta E \rangle, \quad (\text{F4})$$

with the weight function

$$\Theta(u) = \frac{1}{v_r} \frac{dr}{du}. \quad (\text{F5})$$

Taking inspiration from §G of Fouvy et al. (2021), for the Plummer potential, we take our effective anomaly, $u \mapsto r(u)$, to be

$$r(u) = b \sqrt{s^2(u) - 1}, \quad (\text{F6})$$

where

$$s(u) = a(1 + ef(u)), \quad \text{with} \quad f(u) = u \left(\frac{3}{2} - \frac{1}{2} u^2 \right). \quad (\text{F7})$$

In that expression, the effective semi-major axis, a , and eccentricity, e , are defined as

$$a = \frac{s_a + s_p}{2}, \quad e = \frac{s_a - s_p}{s_a + s_p}, \quad (\text{F8})$$

with $s_p = \sqrt{1 + (r_p/b)^2}$ and similarly for s_a . For a given orbit (E, L) , the bounds (s_p, s_a) can be easily computed, as shown in equation (F20). The key motivation of the choice of equation (F6), is that the weight function, $\Theta(u)$ given by equation (F5) becomes explicit and is numerically well-behaved for all $-1 \leq u \leq 1$. Indeed, after simplification, one gets

$$\Theta(u) = \frac{1}{\Omega_0} \frac{3}{4\sqrt{2}} \frac{\sqrt{s_a s_p (s_a + s_p)}}{\sqrt{4 - u^2}} \frac{\mathcal{A}(u)^{3/2}}{\sqrt{s_a s_p \mathcal{A}(u) + \mathcal{B}(u)}}, \quad (\text{F9})$$

with the frequency scale $\Omega_0 = \sqrt{GM/b^3}$. In equation (F9), we also introduced

$$\begin{aligned} \mathcal{A}(u) &= s_p(u+2)(u-1)^2 - s_a(u-2)(u+1)^2, \\ \mathcal{B}(u) &= s_p(u^3 - 3u + 6) - s_a(u^3 - 3u - 6), \end{aligned}$$

which are both always positive. The mapping from equation (F6) is also used to compute the radial period T via

$$\frac{T}{2} = \int_{-1}^1 du \Theta(u). \quad (\text{F10})$$

In practice, to compute the orbit average from equation (F4) we use a midpoint rule with $N_{\text{avg}} = 10^2$ nodes, for which the typical relative error is found to be 10^{-5} .

F3 Action space diffusion coefficients

The orbit-averaged diffusion coefficients in (E, L) -space can finally be converted into action space $\mathbf{J} = (J_r, L)$. To do so, we follow the generic change of coordinates presented in equations (122) and (123) of Bar-Or & Alexander (2016), and write

$$D_{J_r} = \frac{\partial J_r}{\partial E} D_E + \frac{\partial J_r}{\partial L} D_L + \frac{1}{2} \frac{\partial^2 J_r}{\partial E^2} D_{EE} + \frac{1}{2} \frac{\partial^2 J_r}{\partial L^2} D_{LL} + \frac{\partial^2 J_r}{\partial E \partial L} D_{EL}, \quad (\text{F11a})$$

$$D_{J_r L} = \frac{\partial J_r}{\partial E} D_{EL} + \frac{\partial J_r}{\partial L} D_{LL}, \quad (\text{F11b})$$

$$D_{J_r J_r} = \left(\frac{\partial J_r}{\partial E} \right)^2 D_{EE} + 2 \frac{\partial J_r}{\partial E} \frac{\partial J_r}{\partial L} D_{EL} + \left(\frac{\partial J_r}{\partial L} \right)^2 D_{LL}. \quad (\text{F11c})$$

Equation (F11) requires the gradients of J_r with respect to (E, L) . To proceed, we start from the integral definition of J_r (see, e.g., equation 3.224 in Binney & Tremaine 2008)

$$J_r = \frac{1}{\pi} \int_{r_p}^{r_a} dr v_r = \frac{1}{\pi} \int_{-1}^1 du \Theta(u) v_r^2, \quad (\text{F12})$$

with the radial velocity $v_r^2 = 2(E - \psi(r)) - L^2/r^2$, and $\Theta(u)$ following from equation (F9). The first-order derivatives of equation (F12) are naturally given by

$$\frac{\partial J_r}{\partial E} = \frac{1}{\pi} \int_{r_p}^{r_a} \frac{dr}{v_r} = \frac{1}{\pi} \int_{-1}^1 du \Theta(u) = \frac{T}{2\pi}, \quad (\text{F13a})$$

$$\frac{\partial J_r}{\partial L} = -\frac{L}{\pi} \int_{r_p}^{r_a} \frac{dr}{r^2 v_r} = -\frac{L}{\pi} \int_{-1}^1 du \frac{\Theta(u)}{r^2(u)}. \quad (\text{F13b})$$

Similarly, the second-order derivatives read

$$\frac{\partial^2 J_r}{\partial E^2} = \frac{1}{\pi} \int_{-1}^1 du \frac{\partial \Theta}{\partial E}, \quad (\text{F14a})$$

$$\frac{\partial^2 J_r}{\partial L \partial E} = \frac{1}{\pi} \int_{-1}^1 du \frac{\partial \Theta}{\partial L}, \quad (\text{F14b})$$

$$\frac{\partial^2 J_r}{\partial L^2} = -\frac{1}{\pi} \left[\int_{-1}^1 \frac{du \Theta(u)}{r^2(u)} + L \int_{-1}^1 \frac{du}{r^4(u)} \left(\frac{\partial \Theta}{\partial L} r^2(u) - 2b^2 \Theta(u) s(u) \frac{\partial s}{\partial L} \right) \right], \quad (\text{F14c})$$

with $s(u)$ given by equation (F7).

All the gradients appearing in equation (F14) can be obtained using the chain rule and implicit differentiation. Indeed, we write

$$\frac{\partial \Theta}{\partial E} = \frac{\partial s_p}{\partial E} \frac{\partial \Theta}{\partial s_p} + \frac{\partial s_a}{\partial E} \frac{\partial \Theta}{\partial s_a}, \quad (\text{F15})$$

and similarly for $\partial \Theta / \partial L$ and $\partial s / \partial L$. In that expression, the gradients $\partial \Theta / \partial s_p$ and $\partial \Theta / \partial s_a$ follow from equation (F9). Using equations (F7) and (F8), we also have

$$\frac{\partial s}{\partial s_p} = \frac{1}{2}(1 - f(u)), \quad \frac{\partial s}{\partial s_a} = \frac{1}{2}(1 + f(u)). \quad (\text{F16})$$

Now, we must compute the gradients of s_p and s_a with respect to E (and L) entering equation (F15). Energy conservation, $v_r^2 = 2(E - \psi(r)) - L^2/r^2$, in conjunction with the mapping from equation (F6) imposes the constraint

$$E = \frac{E_0}{s_*} + \frac{L^2}{2b^2(s_*^2 - 1)} \equiv \Phi_{\text{eff}}(s_*, L), \quad (\text{F17})$$

q	1	0	-6	-16	-30
N_{run}	100	100	100	50	50
t_{last} [HU]	1000	1000	100	100	100
(N_{J_r}, N_L)	(20,15)	(20,20)	(20,20)	(70,70)	(70,70)
$(J_r^{\text{min}}, J_r^{\text{max}})$	(0, 0.55)	(0, 0.55)	(0, 0.6)	(0, 0.6)	(0, 0.6)
$(L^{\text{min}}, L^{\text{max}})$	(0,1.05)	(0,1.05)	(0,1.1)	(0,1.1)	(0,1.1)

Table G1. Detailed parameters for the N -body simulations and the associated binnings of action space. Following equation (G3), we binned the $\mathbf{J} = (J_r, L)$ action space in $N_{J_r} \times N_L$ uniform bins within the domain $J_r^{\text{min}} \leq J_r \leq J_r^{\text{max}}$ (similarly for L). All quantities are in physical units $G = M = b = 1$ if not stated otherwise.

with $s_* = s_p$ or s_a . When differentiated, equation (F17) gives

$$\frac{\partial s_*}{\partial E} = \frac{1}{\partial \Phi_{\text{eff}} / \partial s_*}, \quad \frac{\partial s_*}{\partial L} = -\frac{\partial \Phi_{\text{eff}} / \partial L}{\partial \Phi_{\text{eff}} / \partial s_*}, \quad (\text{F18})$$

with

$$\frac{\partial \Phi_{\text{eff}}}{\partial s_*} = -\frac{E_0}{s_*^2} - \frac{s_* L^2}{b^2(s_*^2 - 1)^2}, \quad \frac{\partial \Phi_{\text{eff}}}{\partial L} = \frac{L}{b^2(s_*^2 - 1)}. \quad (\text{F19})$$

Finally, for a given value of (E, L) , we must still identify the associated (s_p, s_a) . To do so, we note that equation (F17) can be rewritten as a third degree polynomial in s_*

$$\tilde{E} s_*^3 - s_*^2 + \left(\frac{1}{2} \tilde{L}^2 - \tilde{E} \right) s_* + 1 = 0, \quad (\text{F20})$$

whose three roots are all real and involve the rescaled energy and angular momentum introduced in equation (E2). The product of these roots is $-1/\tilde{E} < 0$, while their sum is $1/\tilde{E} > 0$. As a consequence, this polynomial has one negative root, and two positive ones, namely s_p and s_a . In practice, the search for s_p and s_a was performed using `PolynomialRoots.jl` (Skowron & Gould 2012).

APPENDIX G: N -BODY SIMULATIONS

The simulations presented throughout the main text were performed using the direct N -body code `NBODY6++GPU` (Wang et al. 2015), version 4.1. The initial conditions for the anisotropic Plummer spheres (see equation E1) were generated from `PlummerPlus.py` (Breen et al. 2017), while we used the same input file as in §H1 of Fouvy et al. (2021). Internally, `NBODY6++GPU` uses Hénon units (HU) (Hénon 1971), defined such that $G = M = R_v = 1$ HU, with G the gravitational constant, M the cluster's total mass and R_v its virial radius. For the Plummer potential from equation (8), one readily finds $R_v/b = 16/(3\pi)$ (see, e.g., Table 1 p. 81 in Heggie & Hut 2003). Each N -body realisation was composed of $N = 10^5$ stars and integrated up to $t_{\text{max}} = 1000$ HU with a dump every $\Delta t = 1$ HU. On a 40-core node with a single V100 GPU, one simulation typically required ~ 24 h of computation. In practice, we considered anisotropies set by $q = 1, 0, -6, -16, -30$ and, depending on the values of q , performed either $N_{\text{run}} = 50, 100$ independent realisations, as spelled out in Table G1.

In order to estimate the cluster's instantaneous core radius, $R_c(t)$, we follow the approach from Casertano & Hut (1985). We use $j = 6$ neighbors to estimate the local densities from which we compute the location of the cluster's density centre, $\mathbf{r}_c(t)$, and subsequently the associated core radius, $R_c(t)$ (see equations (II.2)–(II.4) in Casertano & Hut 1985). In Fig. 2, we illustrate the evolution of $R_c(t)$ averaged over the available realisations.

In order to compute the stars' actions, we must pick an appropriate frame. In practice, we centre this frame around the cluster's

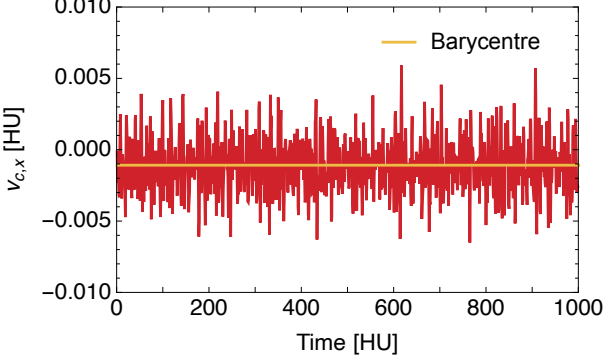


Figure G1. Time dependence of the density centre’s velocity along the x -direction, $v_{c,x}$, for one realisation of the isotropic ($q = 0$) Plummer sphere. The density centre’s velocity is found to closely follow the barycentre uniform motion (orange line).

instantaneous density centre, $\mathbf{r}_c(t)$, and recentre the stars’ velocities with respect to the barycentre uniform motion. In Fig. G1, we check that indeed the density centre’s instantaneous velocity, estimated via $\mathbf{v}_c(t) \simeq (\mathbf{r}_c(t+\Delta t) - \mathbf{r}_c(t-\Delta t)) / (2\Delta t)$, closely follows the barycentre’s uniform velocity.

For a star with (recentered) position and velocity (\mathbf{r}, \mathbf{v}) , we compute its specific energy and angular momentum via

$$E = \psi(\mathbf{r}) + \frac{\mathbf{v}^2}{2}, \quad L = |\mathbf{r} \times \mathbf{v}|. \quad (\text{G1})$$

We subsequently keep only the bound particles, i.e. particles with $E < 0$. Following equation (11), the mean angular momentum, $\langle L \rangle$, is obtained from

$$\langle L \rangle = \frac{1}{N_{\text{bound}}} \sum_i L_i, \quad (\text{G2})$$

where i runs over all the N_{bound} bound particles. Equation (G2) is subsequently averaged over the available realisations to give Fig. 3.

In order to compute the radial action, J_r , at a time t_{last} , we assume that the cluster’s mean potential does not change much from the initial Plummer profile at $t = 0$, and integrate equation (F12) using a midpoint sampling of the effective anomaly u . In order to estimate the relaxation rates, $\partial F / \partial t$, presented in Fig. 4, we bin the (J_r, L) action space with uniform bins. More precisely, for a given action bin of size $\delta J_r \times \delta L$ centered around the action $\mathbf{J} = (J_r, L)$, we compute

$$\frac{\partial F}{\partial t}(\mathbf{J}, t=0) \simeq \frac{F(\mathbf{J}, t_{\text{last}}) - F(\mathbf{J}, t=0)}{t_{\text{last}}}, \quad (\text{G3})$$

where the local DF, $F(\mathbf{J}, t)$, follows from

$$F(\mathbf{J}, t) = \frac{M n(\mathbf{J}, t)}{(2\pi)^3 \delta J_r \delta L}, \quad (\text{G4})$$

$$n(\mathbf{J}, t) = \frac{\text{stars in } [J_r - \frac{1}{2}\delta J_r, J_r + \frac{1}{2}\delta J_r] \times [L - \frac{1}{2}\delta L, L + \frac{1}{2}\delta L]}{\text{total number of bound stars}}.$$

Finally, we average equation (G3) over the available realisations. As highlighted in Fig. 2, the stronger the tangential anisotropy, the faster the cluster’s relaxation, and therefore the smaller the considered time t_{last} to ensure a minimal evolution of the cluster’s mean profile. Similarly, as illustrated in Fig. E1, as the tangential anisotropy increases, the DF gets more concentrated along the $J_r = 0$ axis, which entices us to use smaller action bins. We detail all our binning parameters in Table G1.

In order to compute the ratios defined in equations (12)

and (15), we use a simple midpoint rule. For the NR and P-Iso integrals, given that F and $\partial F / \partial t$ quickly drop away from the cluster’s core, we perform the integrals over the domain $0 < L < L_0$ and $0 < J_r < 0.5L_0$, with $L_0 = \sqrt{GMb}$, using 200 nodes sampled linearly in both directions. For the N -body integrals, we use the exact same bins as the ones used to estimate $\partial F / \partial t$ in equation (G3).

APPENDIX H: MORE ANISOTROPIC SETTINGS

In this Appendix, we complement Fig. 4 by considering Plummer spheres with even stronger tangential anisotropies. This is illustrated in Fig. H1 for $q = -16, -30$. Even in these strongly anisotropic regimes, the anisotropic NR diffusion coefficients from equation (3) predict the structure of $\partial F / \partial t$ in action space, up to an overall prefactor that grows as the anisotropy increases (see Fig. 5).

APPENDIX I: LOCAL CONTRIBUTIONS TO DIFFUSION

In this Appendix, we investigate the differences in the anisotropic and pseudo-isotropic predictions of the local velocity deflections that accumulate as a test star follows its unperturbed orbit. Following equation (9), this is best tracked by considering $(\Delta v_{\parallel}^2)_{\text{loc}}(u) = (\Delta v_{\parallel}^2)(r(u)) \Theta(u)$. This is illustrated in Fig. I1 for a test star orbiting within clusters’ cores with various background velocity anisotropies. As already hinted in Fig. 9, for the range of anisotropies considered here, we recover that the differences between the fully anisotropic NR predictions and the pseudo-isotropic ones are only minor.

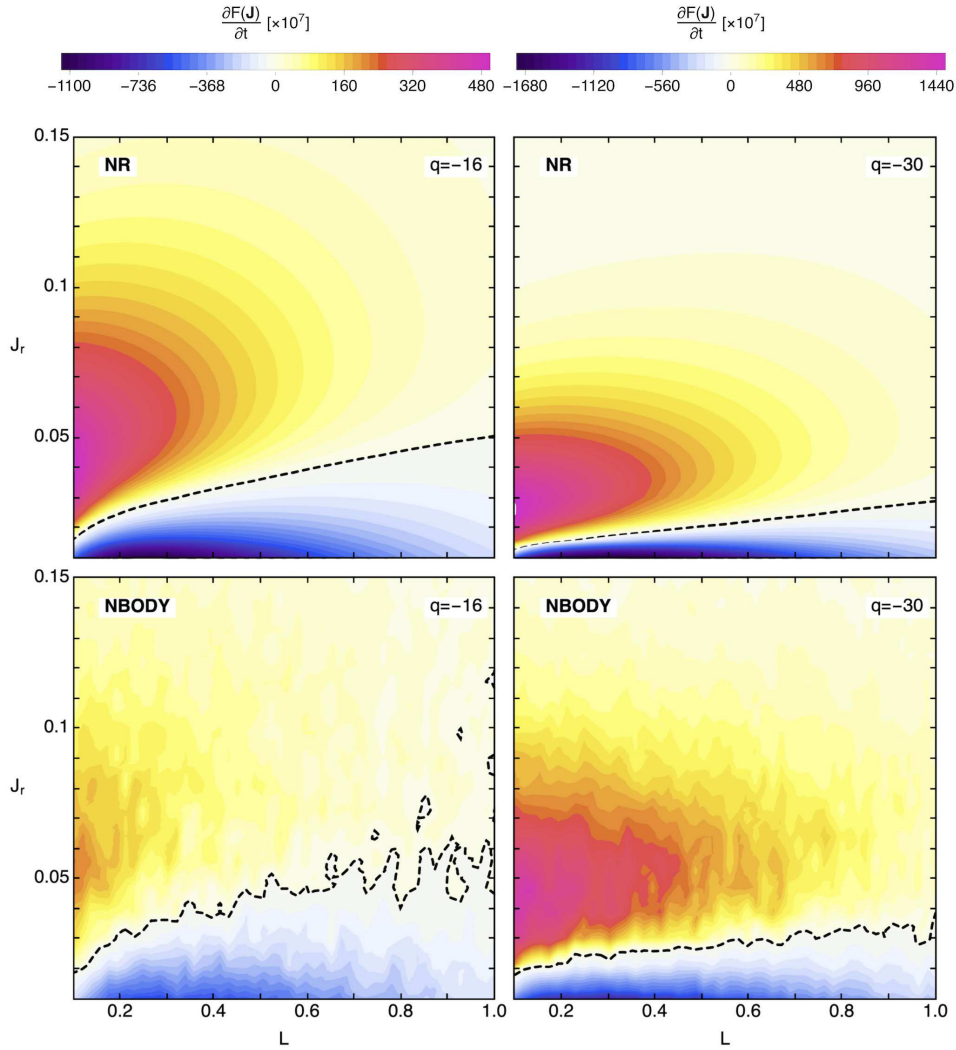


Figure H1. Same as Fig. 4 but for stronger tangential anisotropies. There is a qualitative agreement between the NR predictions and the N -body measurements, up to an overall prefactor that gets larger as the anisotropy increases (see Fig. 5).

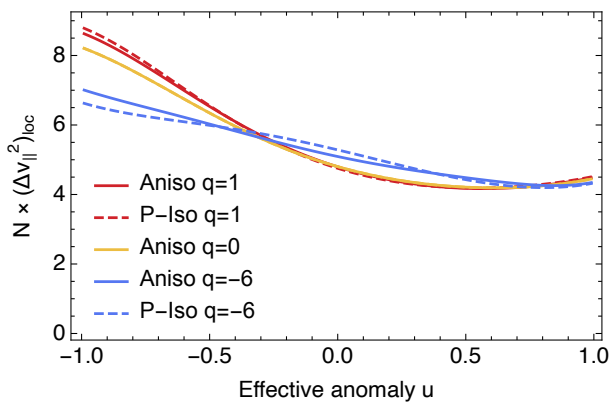


Figure II. Illustration of the velocity deflections accumulated along the motion of a test star, seen here as a function of the effective anomaly u . Full lines are the anisotropic NR predictions (equation 3), while the dashed ones are the pseudo-isotropic ones (equation 14). Different colors correspond to different background velocity anisotropies. The test star's orbit is $J_r = 0.1L_0$ and $L = 0.5L_0$ with $L_0 = \sqrt{GMb}$, and it explores the cluster's core. As in Fig. 10, for the present levels of anisotropies, the differences between the two predictions are minor.